Atmospheric extremes caused high oceanward sea-surface slope triggering the biggest calving event in more than 50 years at the Amery Ice shelf.

Diana Francis [1*], Kyle S. Mattingly [2], Stef Lhermitte [3], Marouane Temimi [4], Petra Heil [5]

[1] Khalifa University of Science and Technology, P. O. Box 54224, Abu Dhabi, United Arab Emirates.

[2] Institute of Earth, Ocean, and Atmospheric Sciences, Rutgers University, New Brunswick, NJ, USA.

[3] Department of Geoscience and Remote Sensing, Delft University of Technology, Mekelweg 5, 2628 CD Delft, Netherlands.

[4] Department of Civil, Environmental, and Ocean Engineering (CEOE), Stevens Institute of Technology, Hoboken, NJ, 07030.

[5] University of Tasmania, Hobart, Tasmania 7001, Australia.

Corresponding Author: diana.francis@ku.ac.ae.

Abstract

Ice shelf instability is one of the main sources of uncertainty in Antarctica's contribution to future sea level rise. Calving events play a crucial role in ice shelf weakening but remain unpredictable and their governing processes are still poorly understood. In this study, we analyze the unexpected September 2019 calving event from the Amery Ice Shelf, the largest since 1963 and which occurred almost a decade earlier than expected, to better understand the role of the atmosphere in calving. We find that atmospheric extremes provided a deterministic role in this event. A series of anomalously-deep and stationary explosive twin polar cyclones over the Cooperation and Davis Seas which generated tides and wind-driven ocean slope leading to fracture amplification along the pre-existing rift, and ultimately calving of the massive iceberg. The calving was triggered by high oceanward sea-surface slopes produced by the storms. The observed record-anomalous atmospheric conditions were promoted by blocking ridges and Antarctic-wide anomalous poleward transport of heat and moisture. Blocking highs helped in (i) directing moist and warm air masses towards the ice shelf and in (ii) maintaining stationary the observed extreme cyclones at the front of the ice shelf for several days. Accumulation of cold air over the ice sheet, due to the blocking highs, led to the formation of an intense cold-high pressure over the ice sheet, which helped fuel sustained anomalously-deep cyclones via increased baroclinicity. Our results stress the importance of atmospheric extremes in ice shelf dynamics via tides and sea surface slope and the

36 need to be accounted for when considering Antarctic ice shelf variability and contribution to sea
37 level, especially given that more of these extremes are predicted under a warmer climate.

38 **Keywords:** Ice shelf calving, icebergs, Amery Ice Shelf, East Antarctica, blocking highs, polar
39 cyclones, explosive cyclones, sea surface slope.

1. Introduction

41 The rapid collapse of several Antarctic ice shelves, observed recently, and the near-instantaneous
42 acceleration of land-ice discharge into the ocean that follows the collapse, demonstrates the
43 sensitivity of the Antarctic cryosphere to recent warming (e.g., Smith et al., 2019; Rignot et al.,
44 2019). However, large uncertainty remains regarding the response of ice shelves to the globally
45 rising temperatures and to the resulting changes in the atmospheric circulation.

46 On 25 September 2019, the Amery Ice Shelf – the third largest ice shelf in Antarctica – calved
47 iceberg D28 (1,636 km2, 210 m thick), which was the largest calving event since the early 1960s
48 (Fig. 1). The Amery Ice Shelf is a key drainage channel in East Antarctica (Fricker et al., 2002)
49 draining roughly 16% of the East Antarctic Ice Sheet (Galton-Fenzi et al., 2012). It is in balance
50 with its surroundings (King et al., 2009; Galton-Fenzi et al., 2012; Li et al., 2020), despite
51 experiencing strong surface melt in summer. However, over the past 20 years, a large system of
52 rifts (a precursor to calving) in the Amery Ice Shelf, known as the Loose Tooth rift system, has
53 been developing (Fricker et al., 2005; Bassis et al., 2008; Darji et al., 2018). Recent studies have
54 shown that the propagation rate of the rifts has been decreasing since 2005 due to increasing
55 thickness of melange ice filling in the rifts, and speculated that forward propagation of the west
56 rift might even stop (e.g., Zhao et al., 2013). Satellite images of the Amery Ice Shelf (Fig. 1) show
57 the largest rift extending in the same direction of the ice flow, widening toward the edge of the ice
58 shelf and from this main rift, with radial rifts extending to the west (T1) and east (T2). Earlier
59 studies predicted that the Amery Ice Shelf would not experience a major calving until around 2025
60 or later. (e.g., Fricker et al., 2002), and the portion that was expected to calve first was T2 i.e., the
61 one to the east of the current calving. This highlights the need for an improved understanding of
62 the underlying processes of calving events and the role of atmospheric forcing as trigger for ice
63 shelf calving.

64 Indeed, most of the mass loss from the Antarctic Ice Sheet – the largest uncertainty for future sea
65 level projections – takes place at the fronts of ice shelves and glacier tongues, via iceberg calving
66 and surface and basal melt (e.g., Pritchard et al., 2012; Shepherd et al., 2018). Compared to
67 melting, rifting and subsequent calving is the fastest way by which marine-terminating glaciers
68 lose mass to the ocean and contribute therefore to sea level rise (e.g., Smith et al., 2019). Despite
69 being floating ice (i.e., changes in their mass due to calving do not have a direct contribution to
70 sea level rise), ice shelves in general act to buttress inland ice by blocking the flow of ice from the
71 interior (Scambos et al., 2008). This restrictive force decreases when ice shelves thin or calve. For
72 example, on the Antarctic Peninsula, such events have been shown to increase by eight-fold the
73 rate of ice flow inland (Rignot et al., 2004; Scambos et al., 2004; 2014). This leads to more ice
74 discharge into the oceans and a consequent increase in the ice-sheet contribution to global sea-
75 level rise (Hogg and Gudmundsson, 2017). Ocean-driven thinning was also detected at key ice

76 shelves of the East Antarctic Ice Sheet including the Amery Ice Shelf (Greenbaum et al., 2015;
77 Smith et al., 2019) suggesting that this region is also susceptible to rapid and large-scale ice loss
78 (Aitken et al., 2016), and could contribute to future sea-level rise (DeConto et al., 2016; Rignot et
79 al., 2019). Therefore, there is a need to assess the sensitivity of East Antarctic ice shelves to
80 atmospheric forcing and to understand the calving processes and their triggers in order to be able
81 to model the future evolution of ice shelves.

82 Beyond being part of a natural glaciological process, calving events at Antarctic ice shelves have
83 been attracting much attention recently (e.g., Liu et al., 2015; Benn and Astrom 2018) as they were
84 found to trigger, in some cases, the total disintegration of the parent ice shelf (Cook and Vaughan
85 2010; Liu et al., 2015; Jeong et al., 2016; Bassis and Ma, 2016; Massom et al., 2018). These events
86 have been attributed mainly to an enhanced regional warming (Vaughan et al., 2012; Pitchard et
87 al. 2012) which increases surface and basal melt as well as to ocean forcing involving intense
88 crevassing and rifting along multiple lines of weakness such as radial crevasses (Liu et al., 2015;
89 Jeong et al., 2016; Bassis and Ma, 2016), to earthquake and tsunami (Brunt et al., 2011) and to
90 regional loss of pack ice in the shelf-front area which allows storm-generated ocean swell to flex
91 the outer margins of the shelves and lead to their calving (Massom et al., 2018). However,
92 atmospheric-dynamics forcing during calving events, particularly the wind mechanical action on
93 rift widening via wind-induced tides and ocean slope, remains unexplored and this the objective
94 of this study.

95 Of particular importance is the impact on Antarctic ice shelves of the poleward shift of
96 extratropical storm tracks (Tamarin and Kaspi, 2017) and the observed increase in the number and
97 intensity of cyclones around Antarctica over the last few decades (Rudeva et al., 2015; Wei and
98 Qin 2016). The poleward shift of extratropical cyclones was found in reanalysis data of recent
99 years (Fyfe, 2003; Son et al., 2008), and models (e.g., Neu et al., 2013) project an estimated
100 poleward shift of cyclone genesis 1° to 2° in latitude on average under enhanced greenhouse gas
101 concentrations (Bengtsson et al., 2009; Barnes and Polvani, 2013). Importantly, this poleward shift
102 was found to be particularly pronounced in the Southern Hemisphere (Pezza et al., 2007; Chang
103 et al., 2012), and the mean intensity of cyclones as well as the number of extreme cyclones are
104 projected to increase under a warmer climate scenario (Lambert and Fyfe, 2006; Ulbrich et al.,
105 2013; Chang, 2017).

106 Changes in cyclone tracks, numbers, and intensity may have significant impacts on Antarctic sea
107 ice and land ice (e.g., Uotila et al., 2011). In fact, weather systems (i.e., cyclones and blocks)
108 resulting from the larger-scale circulation (e.g., Pope et al., 2017) are identified as the main driver
109 of the observed trends in sea ice variability (Matear et al., 2015; Schemm, 2018; Turner et al.,
110 2017; Eayrs et al., 2019). Furthermore, cyclones and their associated atmospheric rivers can induce
111 sea ice melt (Francis et al., 2020) and ice-shelf surface melt (Wille et al., 2019) by virtue of their
112 associated anomalous moisture and heat transport to high latitudes which increase the downward
113 longwave radiation at the ice surface (Woods & Caballero, 2016; Lee et al., 2017; Grieger et al.,
114 2018; Francis et al., 2020). Additionally, cyclones can cause significant sea ice drift (Kwok et al.,
115 2017; Francis et al., 2019a) due to the strong surface winds they carry (Schemm, 2018). Severe
116 storms can generate energetic waves (up to 8 m) in the Southern Ocean capable of penetrating

hundreds of kilometers into the sea ice covered ocean (Kohout et al., 2014; Vichi et al., 2019; Squire, 2020) Concomitantly, the sea ice cover acts as a buffer and attenuates the wave energy over distance (wave amplitude is reduced by several orders of magnitude within 10km of the sea ice edge), reducing therefore the impact of storms on ice shelves (Dolatshah et al., 2018; Massom et al., 2018).

An extreme situation in cyclogenesis is the formation of explosive cyclones. These are developing cyclones for which the central pressure decreases by at least 24 hPa in 24 hours (Sanders and Gyakum, 1980). Explosively developing cyclones are deeper and longer-lasting compared to ordinary cyclones and they are found to be more intense in the Southern Hemisphere than in the Northern Hemisphere (Raele et al., 2019). In particular, explosive cyclones in the Indian Ocean sector of the Southern Ocean (close to South Africa) are stronger and express higher deepening rates than elsewhere around Antarctica (Raele et al., 2019). This same region (between 45°E and 90°E and poleward of 40°S) – encompassing the Amery Basin – stands out in a climatological study (Allen et al., 2010) as one of three main regions for explosive cyclogenesis around Antarctica, where explosive cyclones are characterized by a 20hPa mean pressure depth relative to the surrounding pressure field. A climatological study of explosive cyclones (Lim and Simmonds, 2002) found that the number of explosive cyclones increased in both hemispheres during 1979-1999, and that positive trends of such systems are statistically significant in the Southern Hemisphere. On average, the study identified 26 explosive cyclones per year in the Southern Hemisphere and found that explosive cyclones exhibit greater mean intensity and depth relative to the entire population of ordinary cyclonic systems. A more recent climatological study over a longer period (1979–2013) reported similar findings, with an increase in the frequency of explosive cyclones in the band of 45°–55°S during winter and early spring (Wei and Qin 2016).

The spatial distribution of these cyclones was found to have a close association with that of strong baroclinicity. In general, the preferred region for cyclogenesis is where both a strong temperature gradient and an upper-level trough are present (e.g., Shimada et al., 2014). While high baroclinic instability associated with the horizontal temperature gradient is crucial for the formation and the intensification of cyclones (Davies, 1997, Uccellini, 1990), cyclogenesis occurs only at the entrance and exit regions of upper-level troughs (e.g., Shimada et al., 2014). Around Antarctica, the strongest temperature gradient is found during late winter-early spring along the fringes of the ice pack, making the sea-ice edge a preferred region for cyclogenesis (e.g., Schlosser et al., 2011; Stoll et al., 2018). However, the location of the temperature gradient relative to the ice edge depends strongly on the atmospheric circulation at larger scale, where a strong temperature gradient can occur poleward of the ice edge (i.e., closer to the ice shelves) during an enhanced zonal wave number three (ZW3) pattern (Irving and Simmonds, 2015). This pattern is characterized by the alternation of 3 troughs and 3 ridges around Antarctica. Strong poleward transport of heat and moisture occurs in the ascending branch of troughs and strong equatorward transport of cold air occurs in the descending branch of ridges (e.g., Raphael, 2007). This zonally-alternating pattern of cold and warm air masses creates temperature differences between the different sectors, fuels frontogenesis and promotes the development of explosive cyclones close to the ice shelves and over the sea ice cover.

158 Another aspect of the ZW3 pattern is the impact of the ridges on the propagation speed of the
159 cyclones. In the troughs, the extratropical cyclones and the associated moisture and heat fluxes are
160 directed poleward; once they reach the Antarctic coast they are blocked by the ridges to their east
161 (Francis et al., 2019a; 2020). This results in stationary cyclones over the same region for 1-2 days
162 which in turn induces pronounced impact on the sea ice (e.g., Francis et al., 2019a) and waves
163 (Vichi et al., 2019). The same scenario can happen at the front of ice shelves during winter-spring
164 if the cyclones form closer to the coast and/or the sea ice extent decreases under a warmer climate.
165 Interestingly, the Antarctic sea ice extent has been decreasing since 2015 (Swart et al., 2018) and
166 the ZW3 index has been the most positive on record during the same period (Schlosser et al., 2018;
167 Francis et al., 2019a). Increased warm air advection toward Antarctica was found to be at the origin
168 of the observed negative anomaly in Antarctic sea ice extent in recent years (Schlosser et al., 2018).
169 Given the dual impact of ZW3 circulation on both explosive cyclogenesis (location and intensity)
170 and sea ice extent, this combination may result in a more pronounced impact of extreme cyclones
171 on ice shelves.

172 Another extreme situation in cyclogenesis is the formation of twin cyclones during which the
173 resulting effect of the mutually-interacting cyclones is twice as strong as the individual cyclones
174 (e.g., Moustaoui et al., 2002). To our knowledge, the formation of explosively developing twin
175 cyclones has been, to date, only observed and studied in the tropics (Ferreira et al., 1996;
176 Moustaoui et al., 2002), in the mid-latitudes (Yokoyama and Yamamoto, 2019) and in the Arctic
177 (Renfrew et al., 1997). In this study, we report for the time, the formation of polar twin cyclones
178 near Antarctica during two consecutive events; one on 19-20 September 2019 at 60°E and the
179 second on 23-24 September 2019 at 85°E.

180 Despite the observed poleward shift of extratropical cyclones, the increasing number and intensity
181 of explosive cyclones around Antarctica and the decline in sea ice extent in recent years, the impact
182 of extreme cyclones on ice shelves instability has not been investigated to date.

183 Building on previous studies that investigated these patterns separately, we aim in this study to
184 assess the impact of extreme cyclone activity during the largest calving event since 1963 at the
185 Amery Ice Shelf. Using satellite data and atmospheric reanalyses, we investigate the role of
186 atmospheric forcings in this calving event which occurred under a ZW3-like situation. The
187 development of the explosive cyclones and their impact on sea ice and land ice conditions are
188 addressed in section 2. Section 3 discusses our findings. The data and methods used in this study
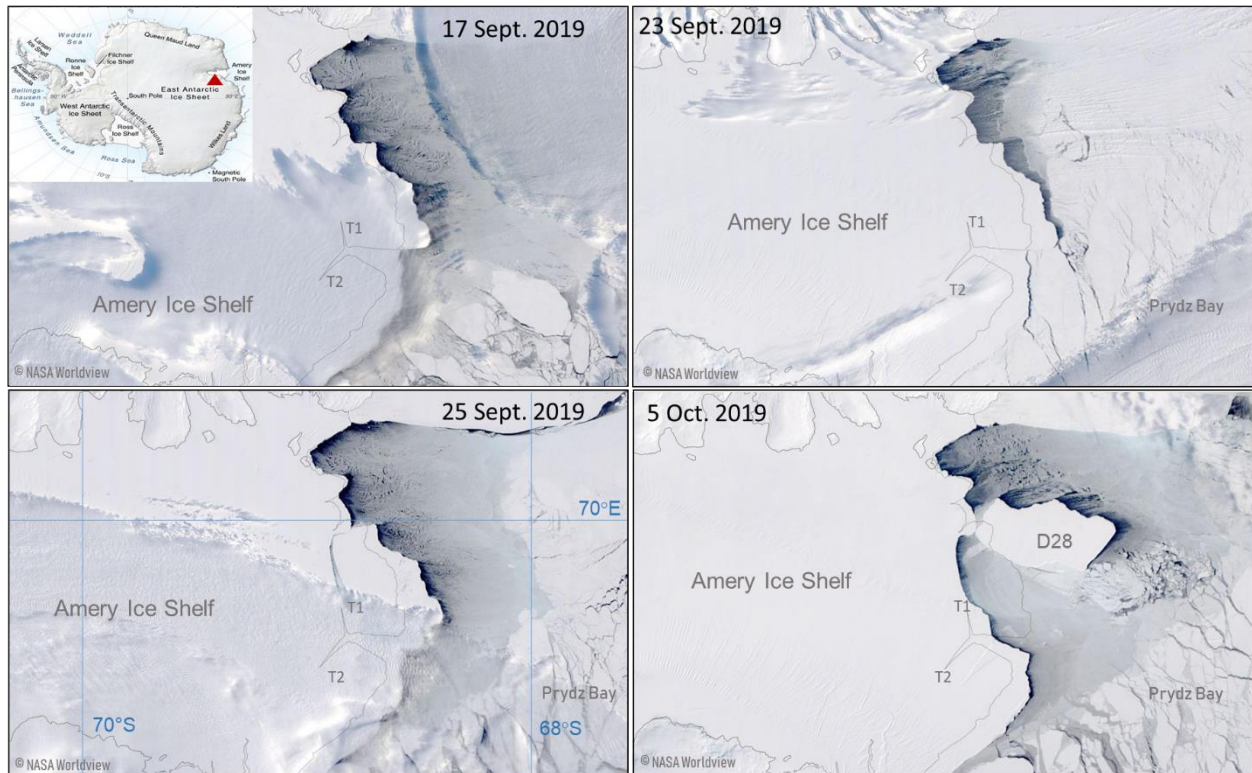189 are described in section 4.

Figure 1: MODIS satellite visible imagery of the Amery Ice Shelf and the Loose Tooth rift system (T1 and T2) at its front. Ice conditions are shown before the calving on 17 and 23 September 2019, during the calving on 25 September 2019, and few days after the detachment of the new iceberg D28. Image credit NASA Worldview.

190

2. Results

2.1 Explosive twin cyclones during 18-22 September 2019 – preconditioning

In September 2019, the synoptic conditions exhibited an amplified zonal wave number 3 (ZW3) pattern characterized by 3 trough/ridge systems associated with low/high mean sea level pressure (MSLP) anomalies. Compared to all Septembers in the 1979-2019 period, the broad scale MSLP anomaly indicates that, for September 2019, there was below average pressure over much of the Antarctic continent and above average pressure to the north (Fig. 2a). In the Indian Ocean sector, the MSLP anomalies exceeded one standard deviation from the mean over large areas with the strongest troughing over Cooperation and Davis Seas (Fig. 2a). To the west of this low pressure anomaly, the South Atlantic ridge exhibited strong positive anomalies exceeding 2 standard deviations from the mean (Fig. 2a). To the east of the low pressure anomaly around the Amery Ice Shelf, another pronounced ridge encompassing south Australia and the Mawson Sea with positive MSLP anomalies exceeded 1 standard deviation from the climatological mean (Fig. 2a).

On a daily scale, the aforementioned synoptic setting was synonym of frequent and extreme weather systems. On 17 September 2019 at 0200 UTC, an extratropical cyclone associated with a 968 hPa low-pressure at its center and located at 60°S, 40°E, started to deepen while moving poleward and eastward. It reached the western side of Cooperation Sea on 18 September 2019 at

208 0200 UTC with a 940 hPa minimum pressure and remained over this region the entire day (Fig.
209 2b), then decayed on 19 September, with 980 hPa central pressure by 1300 UTC. The rapid
210 deepening of the low pressure is characteristic of explosive cyclones (e.g., Sanders and Gyakum,
211 1980). The explosive cyclone on 18 September 2019 was associated with significant poleward
212 transport of moisture (Fig. 2c) and heat (Fig. 2d) carried by an atmospheric river propagating
213 poleward adjacent to the low-pressure center. The atmospheric river was associated with integrated
214 water vapor transport (IVT) greater than 500 kg m^{-1} s^{-1} at its core, with IVT values around 100 kg
215 m^{-1} s^{-1} over Prydz Bay exceeding the 99th percentile of September climatology in this region (Fig.
216 3a). The moisture and heat carried by the atmospheric river over the ice sheet may have caused
217 warming at the surface due to condensation (released heat) as well as by increase in downward
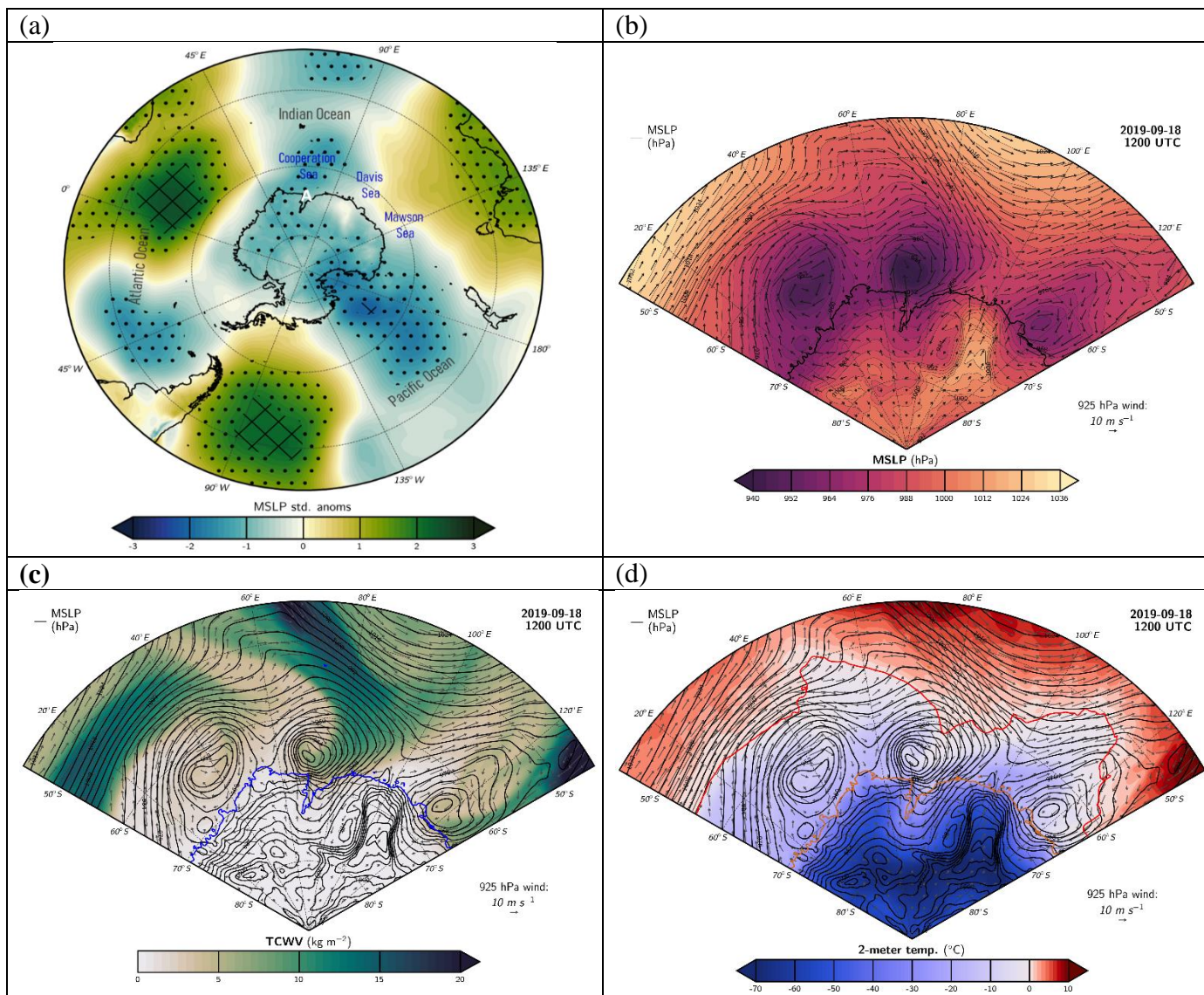218 longwave radiation (e.g., Francis et al., 2020).

Figure 2: Normalized anomalies of Mean Sea Level Pressure (MSLP) for September 2019 relative to the 1979-2019 September climatology. Black dots are regions where the normalized anomalies are larger than 1 standard deviation from the mean and black squares are regions where the normalized anomalies are

larger than 2 standard deviations from the mean. The letter A in white indicates the location of the Amery Ice Shelf. (b) MSLP (shaded) and winds at 925hPa (vectors) at 18 September 2019 1200 UTC, (c) same as (b) but for the total column water vapor (TCWV) in colors, winds at 925hPa in vectors and MSLP in black contours, (d) same as (c) but for 2-m temperature (in colors), winds at 925hPa in vectors, MSLP in black contours and 0°C contour in red.

219

220   In the Southern Hemisphere, where cyclonic winds spin clockwise, the highest wind speed occurs
221   along the bent-back front of the cyclone, i.e., to the west of the low-pressure center of the cyclone
222   (e.g., Wagner et al., 2011, Watanabe and Niino, 2014). This was observed during the explosive
223   cyclone on 18 September 2019 which generated extremely strong surface winds to the west of its
224   center exceeding 20 m s^{-1} (Fig. 3b). Being stationary over Cooperation Sea but to the west of the
225   Amery Basin, this extreme cyclone generated a sustained northeasterly wind stress over the
226   northern part of the ice shelf (Fig. 3b), as well as strong poleward warm and moist air advection
227   (Fig. 2c, 2d and 3a). The combination of warm temperatures brought by the cyclone/AR and strong
228   easterly/northeasterly wind speeds was unusual (Fig. 3). MSLP anomalies during this event were
229   in excess of -4 standard deviations (Fig. 3b), with MSLP values below the 1st percentile of
230   September climatology over a large area along and to the north of the ice shelf margin (Fig. 3b).
231   Extreme wind anomalies exceeding the 99th percentile over the central and eastern ice shelf margin
232   were associated with this cyclone from 18 September through 19 September 2019 (Fig. 3c).
233   Surface winds of 25 m s^{-1}, relative to 99 percentiles (5 standard deviations above the climatological
234   mean), were registered during this event (Fig, 3b and 3c). Likewise, there were sustained positive
235   2-m temperature anomalies throughout the period exceeding 2 standard deviations from the
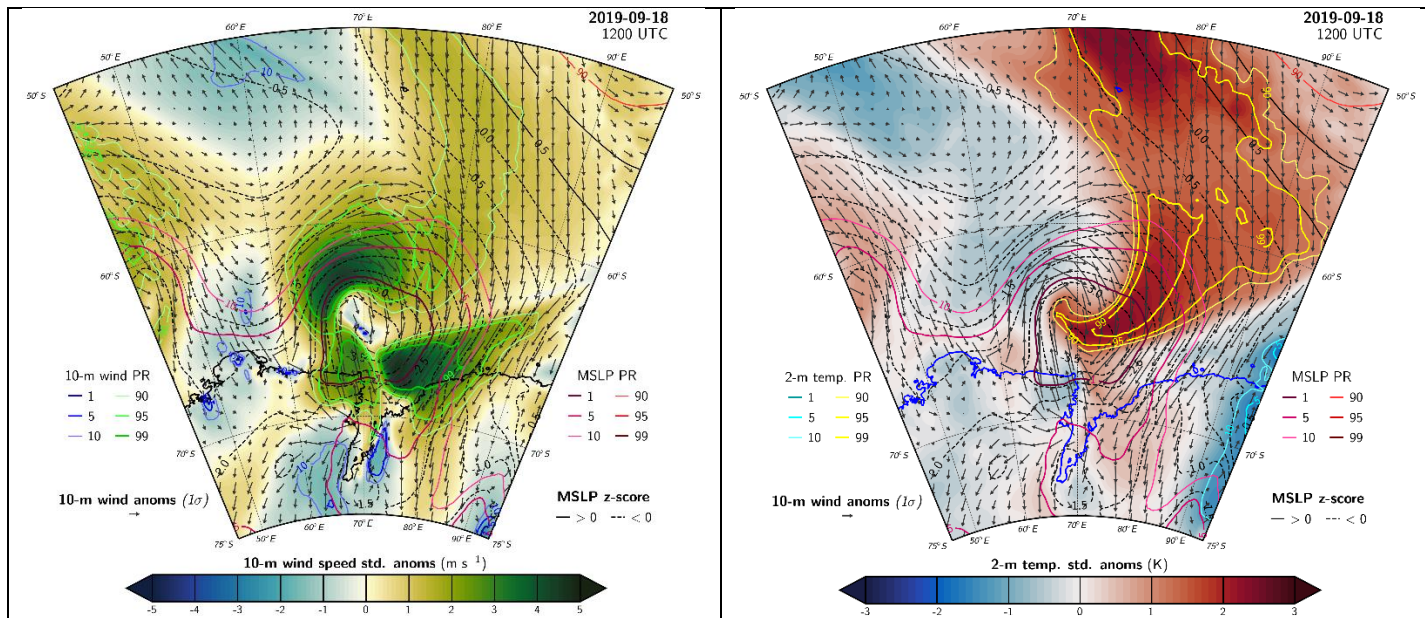236   climatological mean (Fig. 3d).

237
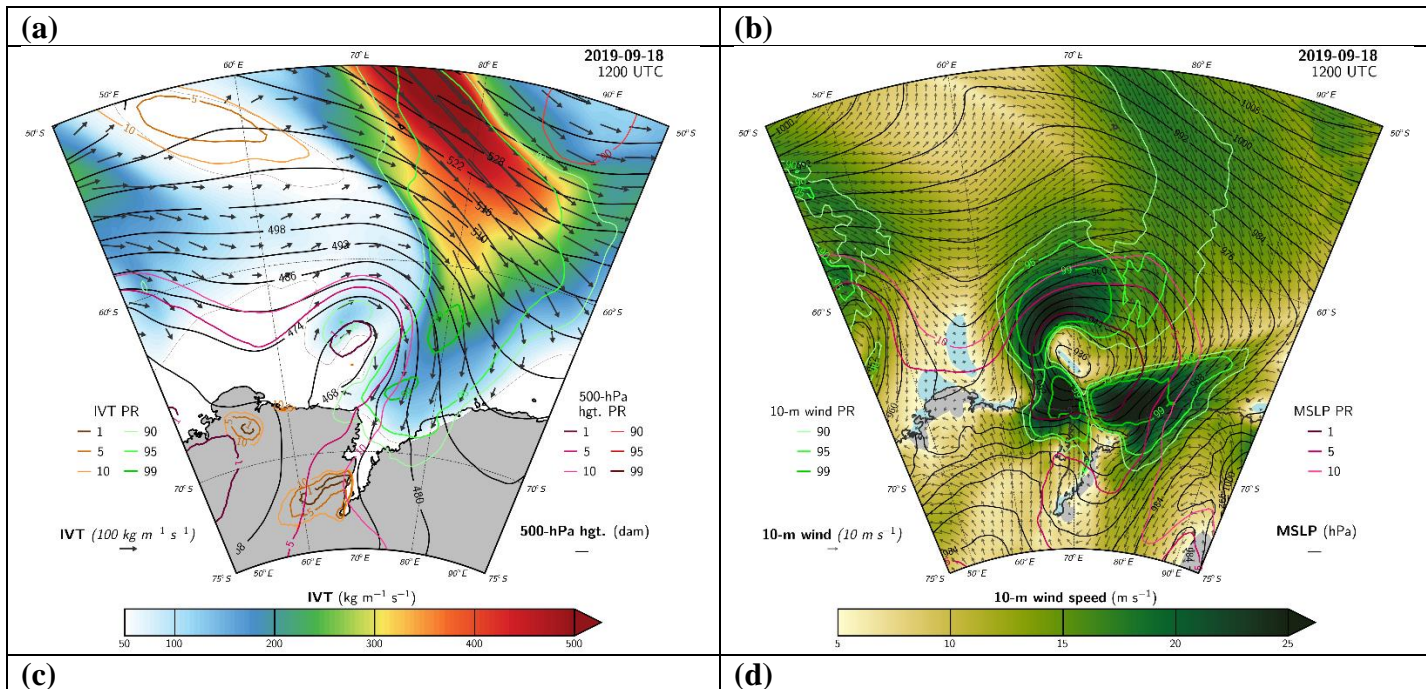
Figure 3: Maps on 18 September 2019 at 1200 UTC of (a) Integrated water vapor transport (IVT) shaded, geopotential heights at 500 hPa in black contours and IVT direction in black vectors, (b) 10-m wind speed in colors, 10-m wind direction in black vectors and MSLP in black contours. (c) Standardized 10-m wind speed anomalies relative to the full September record (1979-2019) (d) Same as (c) but for 2-m temperature. Colored contour lines show percentile rank extremes (1, 5, 10 and 90, 95, 99 percentile ranks) of the corresponding quantities indicated on the plots. On (c) and (d): Vectors show 10-m wind anomalies, black contours show positive MSLP anomalies and dashed black contours show negative MSLP anomalies.

238

The first explosive cyclone on 18 September 2019 was followed immediately by a second explosive cyclone which approached Cooperation Sea from the west on 19 September at 1400 UTC with a deep low of 952hPa. At 2000UTC, this deep cyclone widened and evolved into two twin polar cyclones over the same region (Fig. 4a). The twin cyclones exhibited 960hPa low-pressure at their respective centers and remained active to the west of the Amery Ice Shelf for three consecutive days (Fig. 4a). Their signatures dissipated in the pressure field on 22 September 2019 at 0000UTC. The poleward transport of heat (Fig. 4b) and moisture (Fig. 4c) towards the Amery Ice Shelf continued during this event together with extreme wind stress exceeding the 99th percentile (Fig. 4d). Being stationary to the west of the Amery Ice Shelf (Fig. 4a), the twin cyclones induced extreme easterly winds across the ice shelf, with u-wind anomalies exceeding -5 standard deviations of September climatology over the western ice shelf from 19 September 2019 at 1900 UTC through 20 September at 1100 UTC (Fig. 4d) and below the 1 percentile u-wind values over the whole lower ice shelf area (Fig. 4d). When compared with the climatology for all months during 1979-2019, many hourly wind speeds over the ice shelf front during 18-20 September were substantially greater than the 99th percentile of climatology, with the most anomalous wind speeds on 18 September (Fig. 6e).

On 21 September 2019, the twin cyclones merged and moved to the area in front of the Amery Ice Shelf (Fig. 4e) resulting in a deep cyclone associated with MSLP at its center below the 5th percentile. The remnant cyclone slowly moved along the northern margin of Prydz Bay and

258 decayed on 22 September 2019. Anomalously warm air masses were brought by this cyclone over
259 the margins of the Amery Ice Shelf exceeding the 90th percentile (Fig. 4e). MODIS satellite
260 imagery on this day showed a swirling cyclone at the mouth of the Amery Ice Shelf (Fig. 4f).
261 Sentinel-3A and 3B observations on 22 September 2019 at 0000 UTC (i.e., during the decay of
262 the cyclones) show elevated sea surface at the ice-shelf front area reaching 6 m significant wave
263 height (Fig. 4g). Given the easterly direction of the winds associated with the storm during this
264 episode, the observed elevation of sea surface indicates that storm tide occurred at the ice shelf
265 front. Furthermore, waves and tides generated by the cyclones during the 18-21 September 2019
266 period, when easterly wind speeds were stronger, may have been substantially higher.
267 Unfortunately, sentinel observations are not available during this period over the area of interest
268 to check this.

269 Surface melt during this event may have occurred briefly due to the anomalous warm and moist
270 air masses. However, the inspection of daily satellite images of Sentinel-1 backscatter coefficient,
271 MODIS ice surface temperature and AMSR2 brightness temperature did not show any prolonged
272 nor significant surface melt at the Amery Ice Shelf during this event.

273 In summary, an extended period of strong cyclonic activity from 18-22 September 2019 resulted
274 in exceptional period of strong easterly / northeasterly winds over the western side of the Amery
275 Ice Shelf where the climatology shows a positive zonal component. These exceptional winds
276 generated significant storm surge onto the ice shelf and helped in preconditioning the breakoff as
277 it will be discussed in section 2.3.
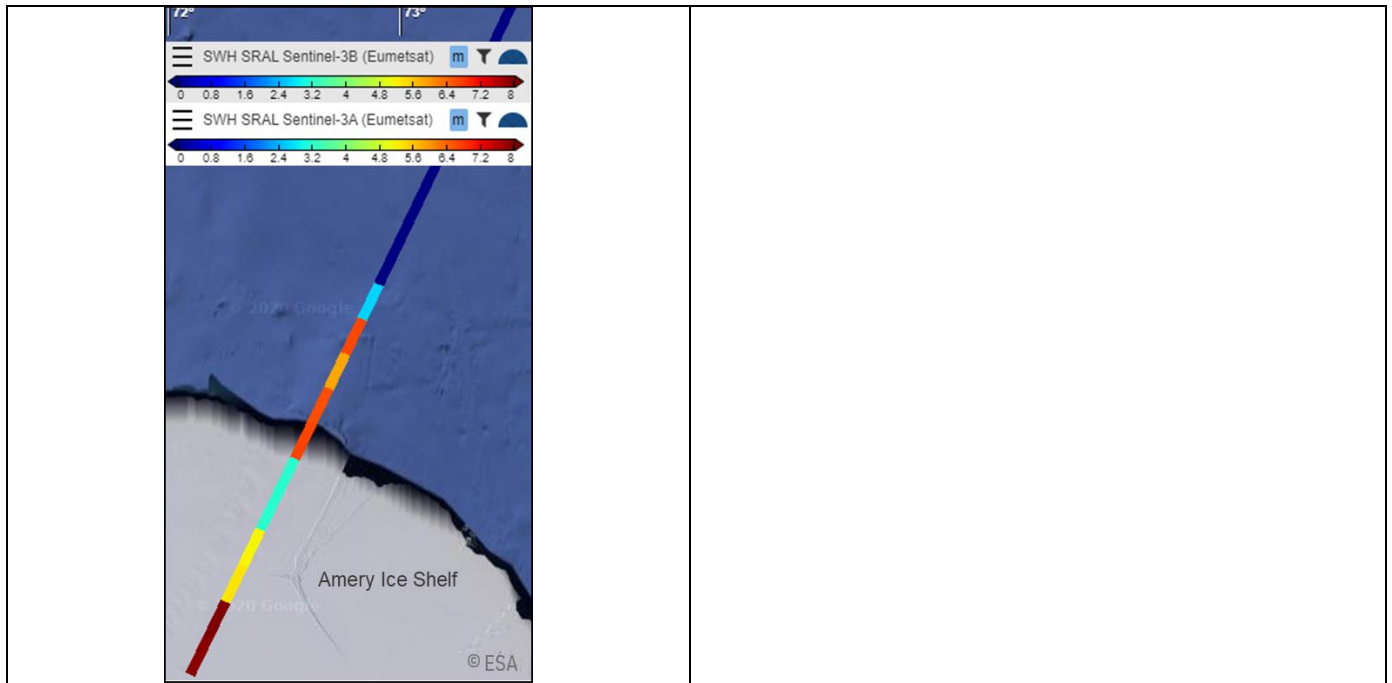
278 .

279

(e)

(f)

(g)
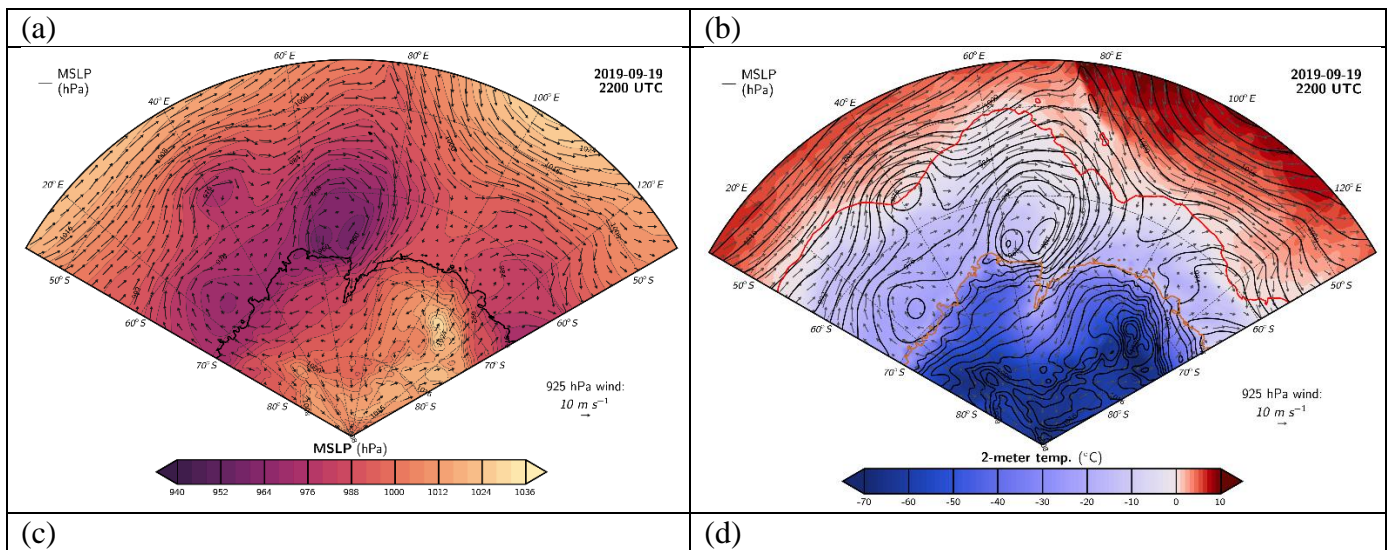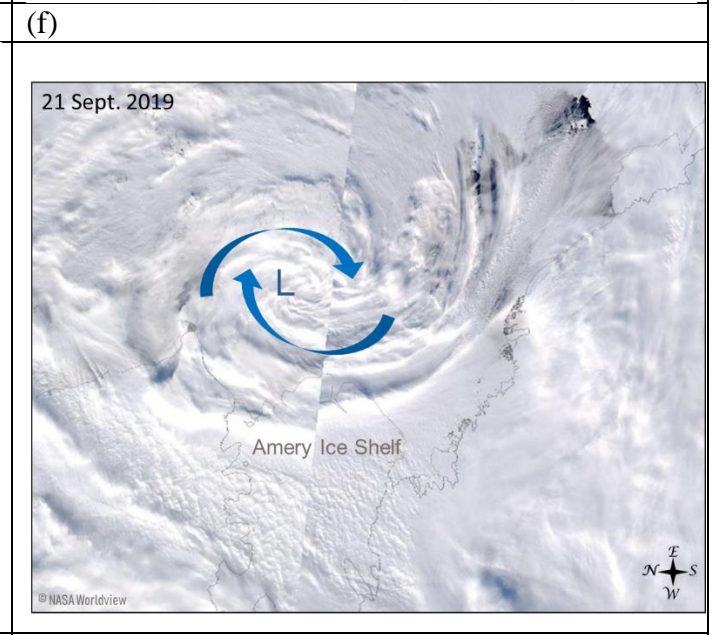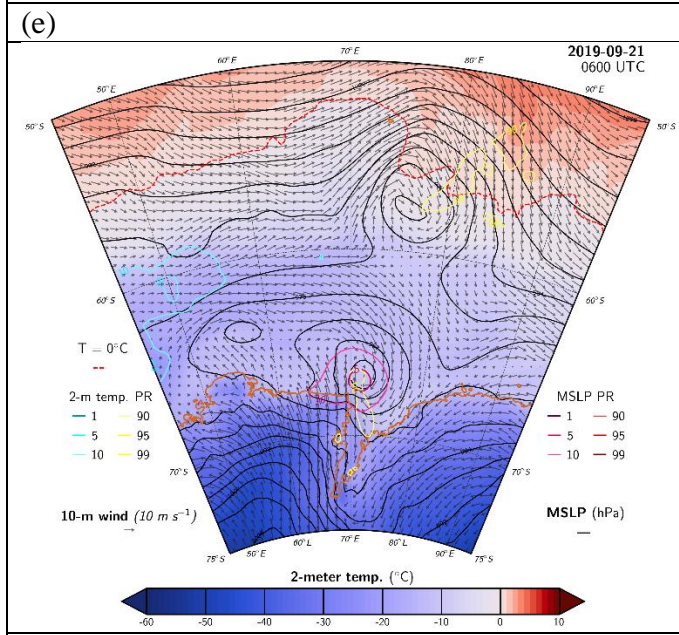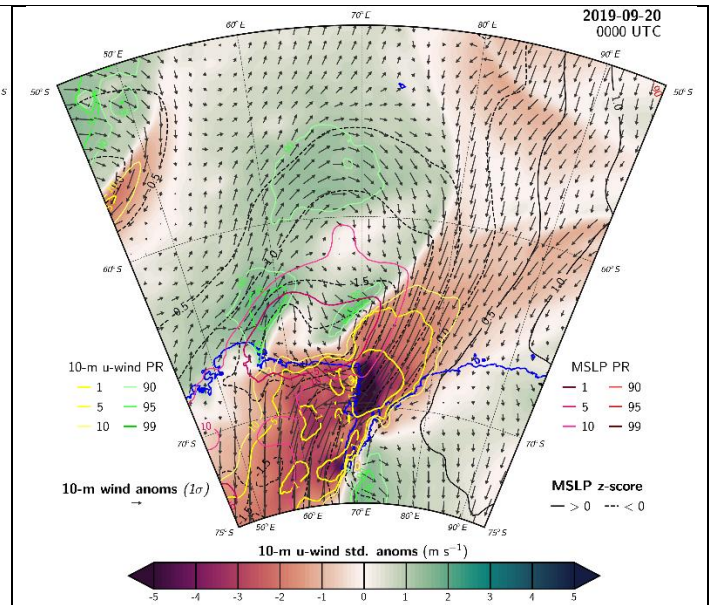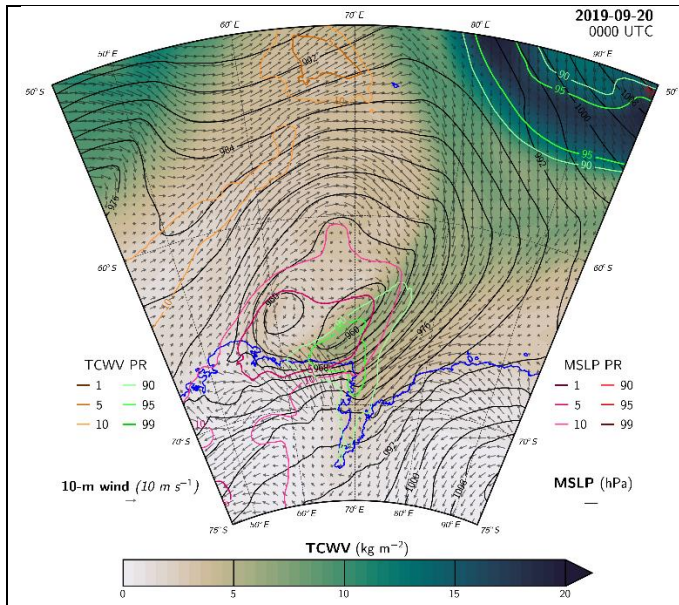
Figure 4: ERA5 reanalysis of: (a) MSLP in colors and winds at 925hPa in vectors on 19 September 2019 at 2200 UTC, (b) 2-m temperature in colors, winds at 925hPa in vectors, MSLP in black contours and 0°C contour in red on 19 September at 2200 UTC, (c) total column water vapor (TCWV) in colors, winds at 925hPa in vectors and MSLP in black contours on 20 September 2019 at 0000 UTC, (d) standardized anomalies relative to the full record (1979-2019) of 10-m u-wind on 20 September 2019 at 0000 UTC. Vectors show 10-m wind anomalies, black contours show positive MSLP anomalies and dashed black contours show negative MSLP anomalies. Colored contour lines show percentile rank extremes (1, 5, 10 and 90, 95, 99 percentile ranks) of the corresponding quantities indicated on the plots, (e) 2-m temperature in colors, 10-m winds in vectors, MSLP in black contours and 0°C contour in red dashed-line on 21 September at 0600 UTC. (f) MODIS visible imagery on 21 September 2019, image credit: NASA worldview. (g) Sentinel-3A and 3B observations of wave height on 22 September 2019 at 0000 UTC, image credit: ESA Ocean Virtual Laboratory.

280

## 2.2. Twin polar cyclones during 23-24 September 2019 - calving

Following the extended period of extreme cyclones in Cooperation sea, an explosive cyclone started to develop on 21 September 2019 centered at 45°E and 60°S. The pressure at its center deepened from 976hPa on 21 September at 1900 UTC to 952hPa on 22 September 2019 at 19 UTC (not shown). On 23 September 2019, the large explosive cyclone entered Cooperation Sea from the west with a deep low of 940 hPa (Fig. 5a). It was accompanied by an intense atmospheric river exhibiting core IVT greater than 800 kg m^{-1} s^{-1} and stretching from mid-latitudes towards Antarctica (Fig. 5b). The explosive cyclone was stationary over Cooperation Sea during the whole day on 23 September 2019, being trapped between two far-south-reaching blocking highs one to the west of it and the second to its east (Fig. 5a and 5c). The cyclone intensified, increased in size and evolved into twin cyclones on 24 September 2019 at 0000 UTC associated with 952hPa low pressure at their respective centers (Fig. 5c and 5d). The mutual interaction between the two cyclones appeared as co-rotation and an eastward translation of the binary pair by the ambient

flow. The interplay between the cyclones lasted for one day after which the twins merged and decayed on 25 September 2019.

To the south of the twin cyclones, a cold pressure high (1036 hPa) developed over the ice sheet as a result of the accumulation of cold air due the blocking ridge to the northeast (Fig. 5c). The high-pressure advected very cold air (2-m temperature below -40°C) into the twin-cyclone system (Fig. 5e and 5 f) which may have fostered baroclinicity and frontogenesis, hence sustaining the twin cyclones for a longer period of time.

The atmospheric river continued to advect large amounts of moisture and precipitation occurred over a large area (Fig. 5d). Sustained advection of exceptionally warm air masses was observed during this event as well (Fig. 5e and 5f). Air masses characterized by 0°C 2-m temperatures were seen to penetrate further south reaching 66°S over the region to the east of the twin cyclones during the whole day on 24 September 2019 (Fig. 5e and 5f).
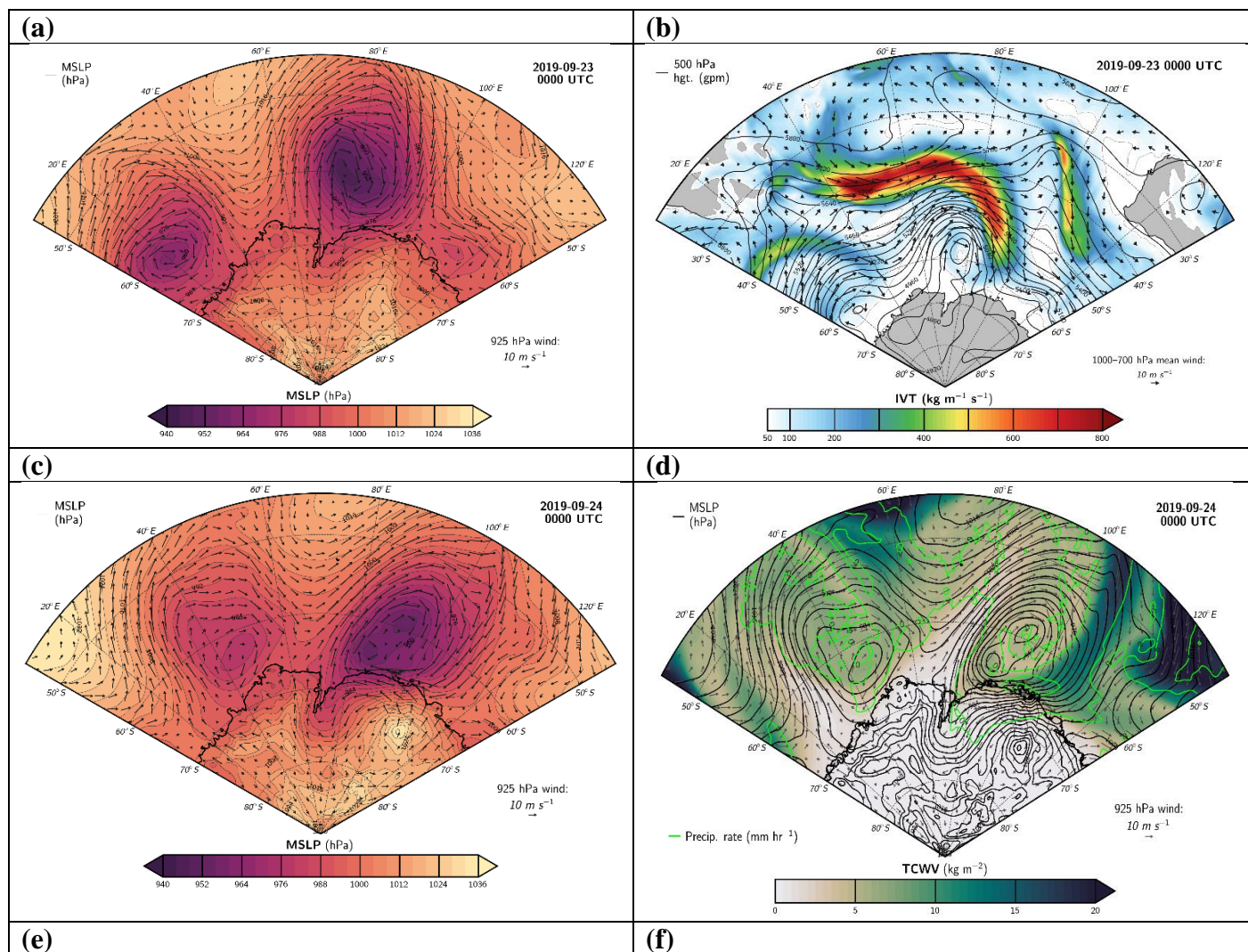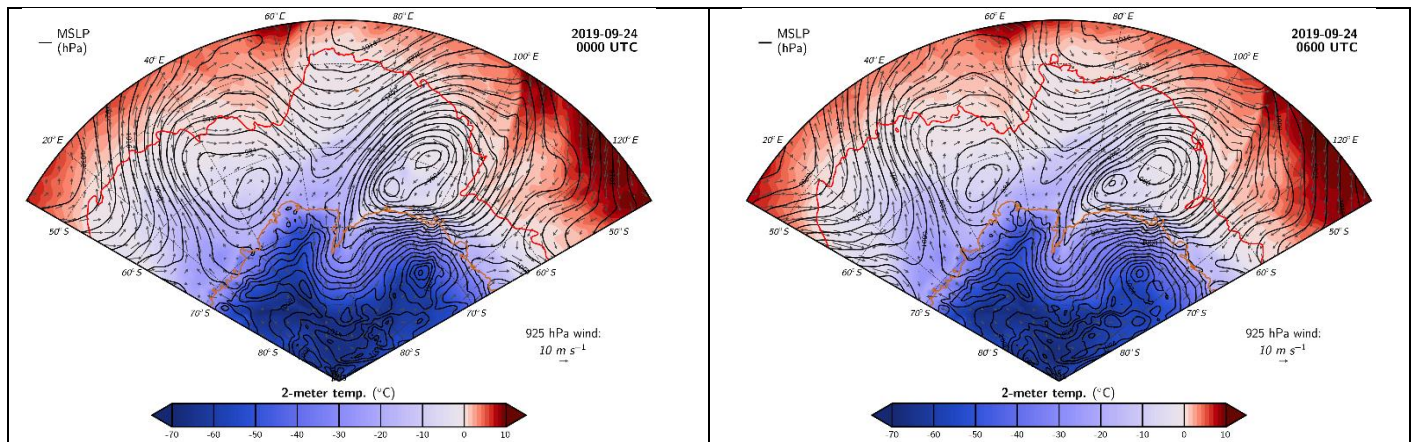
Figure 5: (a) MSLP in colors and winds at 925hPa in vectors on 23 September 2019 at 0000 UTC, (b) integrated water vapor transport (IVT) in colors, geopotential heights at 500 hPa in black contours and 1000-700 hPa mean winds in black vectors on 23 September 2019 at 0000 UTC, (c) MSLP in colors and winds at 925hPa in vectors on 24 September 2019 at 0000 UTC, (d) total column water vapor (TCWV) in colors, winds at 925hPa in vectors, precipitation rate in green contours and MSLP in black contours on 24 September 2019 at 0000 UTC, (e) 2-m temperature in colors, winds at 925hPa in vectors, MSLP in black contours and 0°C contour in red on 24 September at 0000 UTC, (f) same as (e) but at 0600 UTC.

During 23-24 September, the deep twin polar cyclones were stationary to the east of the Amery Ice Shelf (Fig. 5) associated with MSLP anomalies at their centers below the 5th percentile (Fig. 6a and 6c). They induced extreme westerlies (10-m wind speed in the order of 17 m s^{-1}) across the ice shelf with positive 10-m wind anomalies exceeding 2 standard deviations from the climatological mean (Fig. 6a). The direction of the winds was also exceptional with above 99th percentile u-wind over the western ice shelf margin from 23 September 2019 at 1800 UTC (Fig. 6b) through 24 September 2019 at 1200 UTC and below the 5th percentile u-wind values over the lower eastern ice shelf area (Fig. 6a and 6b). Weaker but still significant (95 percentile) westerly wind anomalies lingered during the remainder of the day on 24 September 2019 and through midday on 25 September 2019 with wind speed at 10-m reaching 15 m s^{-1} at the front of the ice shelf (Fig. 6d). Sustained positive 2-m temperature anomalies were observed throughout the twin cyclone event over the eastern side of Prydz Bay. Warm air advection by the twin cyclones brought 95 percentile rank temperatures over the eastern side of the Amery Ice Shelf and Prydz Bay on 23 and 24 September 2019 and 90 percentile rank temperatures inland over Princess Elizabeth Land (Fig. 6c). These episodes of poleward advection of warm air masses may explain the observed positive-trend in surface temperatures during winter/spring seasons at Prydz Bay reported by Heil (2006) using measurements from ground stations.

The distribution of hourly 10-m wind speed for all months 1979-2019 over the Amery Ice Shelf front is shown in the histogram in Fig. 6f. The winds during the 18-22 September 2019 period were exceptionally unusual compared to the record. The winds during the 23-25 September 2019 period were strong but not unusually extreme. This suggests that the first extreme cyclones' event had an important role in preconditioning the ice shelf front for breakoff, while the offshore winds during the second event triggered the calving along the T1 rift.

14

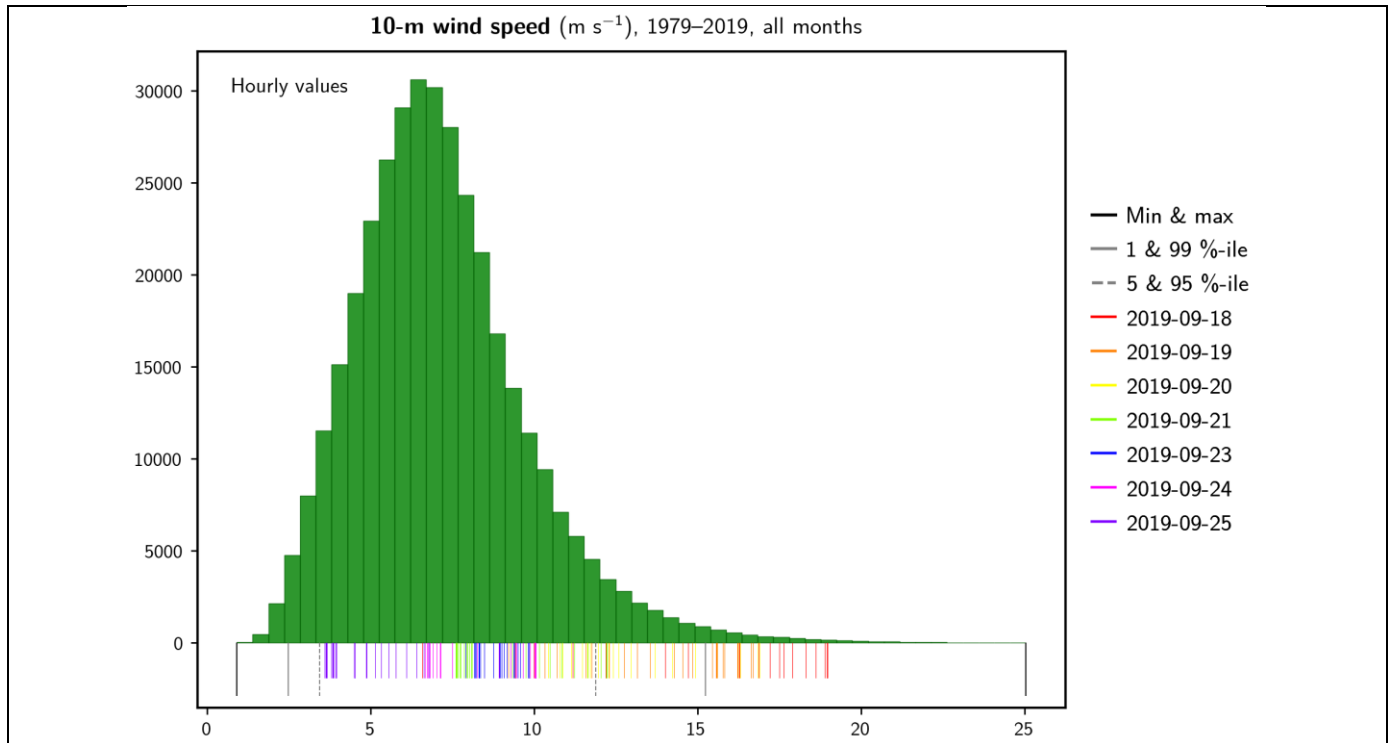**10-m wind speed** (m s^{-1}), 1979–2019, all months

Hourly values
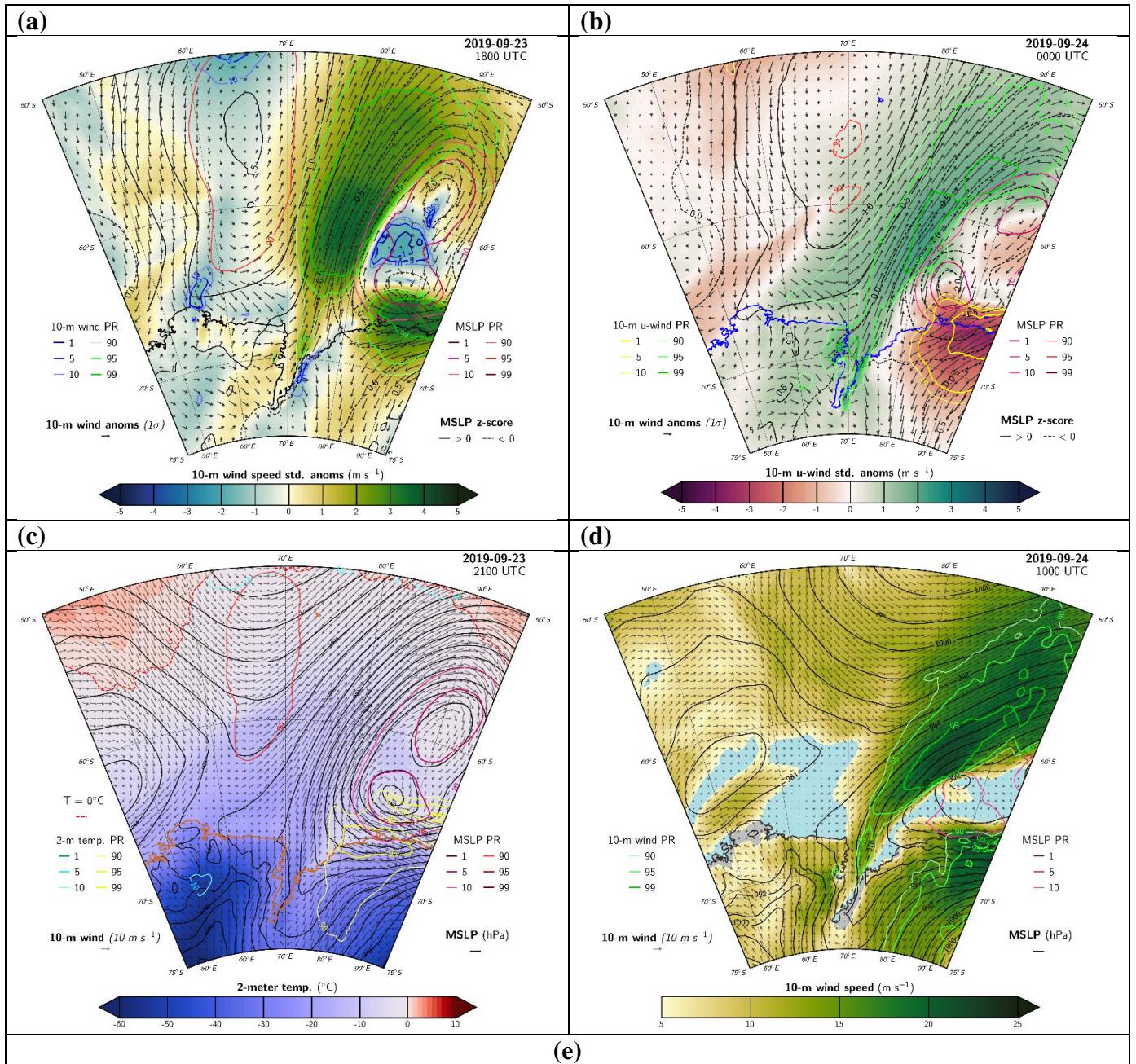
Figure 6: (a) Standardized anomalies relative to the full September record (1979-2019) of 10-m wind speed (colors) at 23 September 2019 1800 UTC. (b) Same as (a) but with u-component of 10-m wind as filled contours at 24 September 2019 0000 UTC. Vectors show 10-m wind anomalies, black contours show positive MSLP anomalies and dashed black contours show negative MSLP anomalies. Colored contour lines show percentile rank extremes (1, 5, 10 and 90, 95, 99 percentile ranks) of the corresponding quantities indicated on the plots. (c) 2-m temperature in colors, winds at 925hPa in vectors, MSLP in black contours and 0°C contour in red dashed-line on 23 September at 2100 UTC. (d) 10-m wind speed in colors, 10-m wind direction in black vectors and MSLP in black contours on 24 September 2019 at 1000 UTC. (e) Histogram showing the distribution of hourly 10-m wind speed for all months during 1979-2019, spatially averaged over 70-65°S and 70-75°E. The colored vertical lines correspond to hourly values during the 18-25 September 2019 period. Each given day in September 2019 has 24 hourly values plotted in the same color.

2.3 The calving

The anomalous atmospheric conditions during the extended period of strong cyclonic activity occurring over the ice cover in Cooperation and Davis Seas (i.e., south to the sea ice edge) impacted the state of the ocean in front of and around the Amery Ice Shelf. The storm surge caused by the first twin cyclones (i.e., Fig. 4g) was followed by an ocean ward slope induced by the second episode of cyclones. Fig. 7a shows a clear increase in maximum ocean slope close to the Amery Ice Shelf in the period prior to the calving (0.05 degrees slope anomaly). The wind pattern of 23-24 September induced a significant slope on the ocean surface at/near the ice front. This ocean ward slope tugs on the ice front, placing extensional stress on the pre-existing rift. The SAR satellite image on 23 September 2019 together with the ice-displacement velocity (rate and direction in vectors) relative to 11 September 2019 are shown in Fig. 7b. The displacement vectors

16

indicate that the iceberg-to-be was rotating in the period 11-23 September 2019 prior to the calving. Wind-induced ocean slope caused a leftward (relative to the rift T1) splitting-movement of the future iceberg prior to break-off on 25 September 2019. This caused rapid opening of the crack and subsequent movement of the iceberg away from the ice shelf (Fig. 8a).

The extreme nature and long duration of the cyclones during both cyclones' episodes resulted in sustained tides and ocean ward slope of the sea surface, consecutively. Between the previous storm event and the 23-24 September storm, there was a rapid change from a shoreward surge to ocean slope away from the ice front. This put strain on the pre-existing rift at the front of the Amery Ice Shelf leading to rift growth and calving.
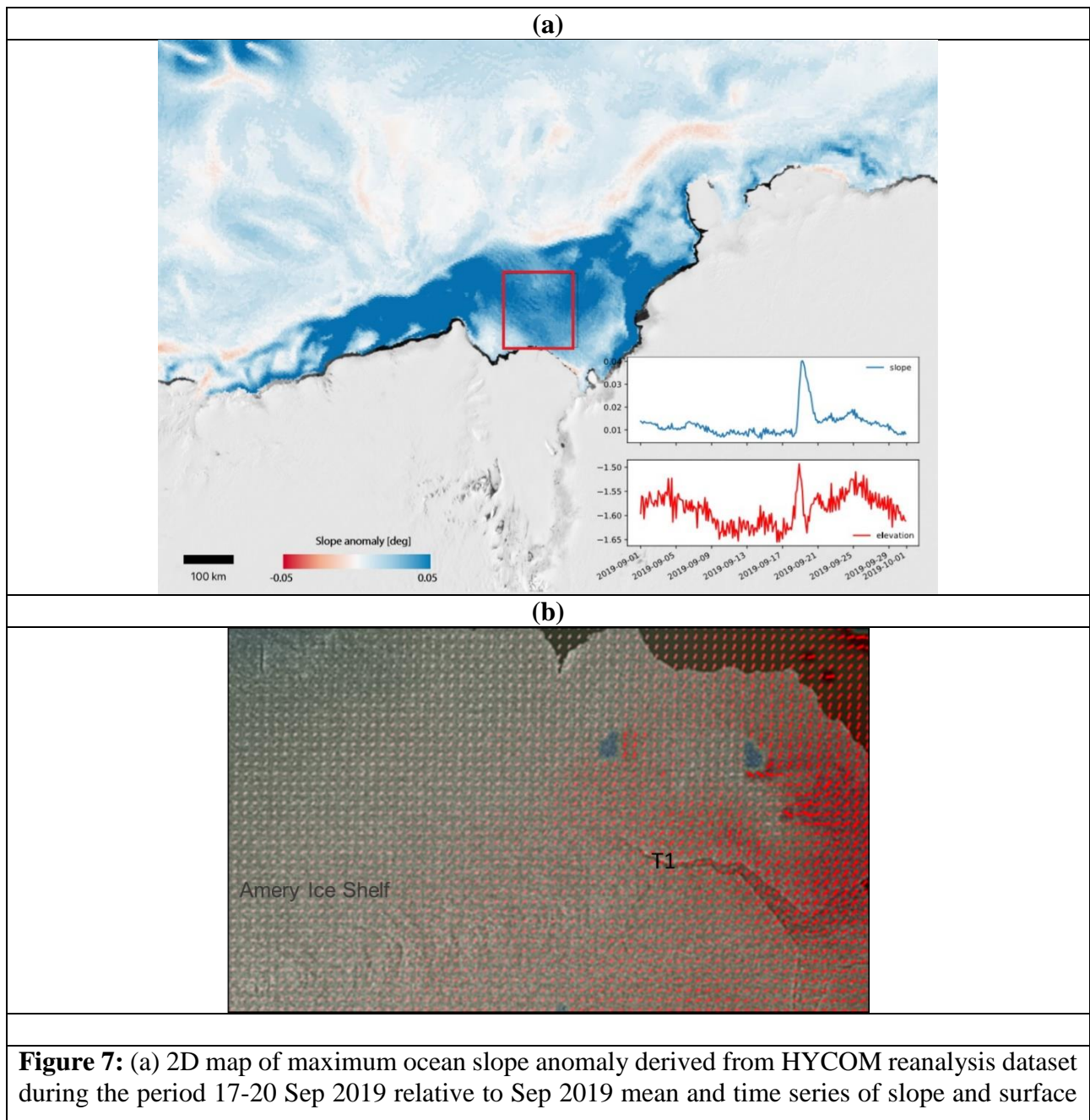

Figure 7: (a) 2D map of maximum ocean slope anomaly derived from HYCOM reanalysis dataset during the period 17-20 Sep 2019 relative to Sep 2019 mean and time series of slope and surface

elevation over the red bounding box showed on the map. (b) SAR image of the Amery Ice Shelf on 23 September 2019. The red vectors correspond to the ice displacement on 23 September 2019 (both velocity and direction) relative to 11 September 2019.

2.4 Sea ice conditions

The action of strong winds on sea ice removal from the area at the mouth of the Amery Ice Shelf was visible in MODIS imagery as well as in the satellite observations of sea ice concentration and drift (Fig. 8). During the period of the twin polar cyclones on 23- 24 September 2019, the sea ice was pushed about 65 km away from the ice shelf front in just a 2-day period of time (Fig. 8a). The ice-free region in front of the ice shelf presented an asymmetric shape where the sea ice in front of the western side of the ice shelf was pushed further away compared to the sea ice in front of the eastern side (Fig. 8a). This may have made the western side more vulnerable to the winds and associated tide/ocean slope induced by the consecutive explosive cyclones.

Moreover, sea ice concentration in Cooperation Sea and at the Amery Ice Shelf front area was reduced to below 60%, reaching 40% in some places (Fig. 8b and 8c). By the end of the intense cyclonic activity period, areas of open water formed especially at the locations of the strongest surface winds i.e., to the west of the twin cyclones centers (Fig. 8b and 8c). Significant reduction in sea ice concentration was also observed along the sea ice edge associated with wind-driven currents and waves (Fig. 8b).

Significant sea ice drift was observed at the mouth of the Amery Ice Shelf associated with the exceptional westerlies generated by the twin cyclones on 23-24 September 2019 (Fig. 8c). The sea ice drift velocity during this period reached 50 km on average per day and the sea ice drifted away from the Amery Ice Shelf towards the east and northeast (Fig. 8c).

Sea ice loss in the vicinity of weakened or flooded shelves is considered as a contributor factor to rapid ice shelf calving (e.g., Massom et al., 2018). The removal of the protective buffer represented by sea ice for ice shelves (e.g., Massom et al., 2018) may have increased the effect of the ocean ward slope on the outer ice shelf western margin and helped in the gravitationally-induced calving.

Explosive cyclones crossing the sea ice zone around Antarctica can generate waves of up to 8 meters in height that are capable of propagating more than 100 km into the sea ice cover (Vichi et al., 2019). The consecutive deep cyclones under scrutiny impacted immediately the Amery Ice Shelf front since they were found very close to the coast. During the first period of explosive twin cyclones, the cyclones were sitting to the west of the Amery Ice Shelf which directed anomalous warm and moist easterlies towards it. This situation caused shoreward storm surge and tide immediately at the shelf front (Fig. 4g). This was then followed by additional extreme atmospheric forcing brought by the second event of explosive twin cyclones, producing strong offshore winds, sea ice removal and ocean ward sea surface slope. This combination of factors weakened the ice shelf front and made it more vulnerable, resulting in amplification of the fractures along the pre-existing rifts and leading ultimately to its calving.

Previous studies (Holdsworth and Glynn, 1978; Squire et al., 1994) have shown that calving ice shelves can be triggered by wind-induced waves which impose flexural strains on the ice shelves,

390 with the potential to induce crevasse and rift propagation and calving (Robinson and Haskell, 1992;
391 Bromirski et al., 2010). This effect can be even maximized by the loss of the protective sea ice
392 pack at the front of the ice shelves (Massom et al., 2018). Here we have shown that the series of
393 intense cyclones provided ideal conditions for both sea ice reduction, wind-tides and ocean slope
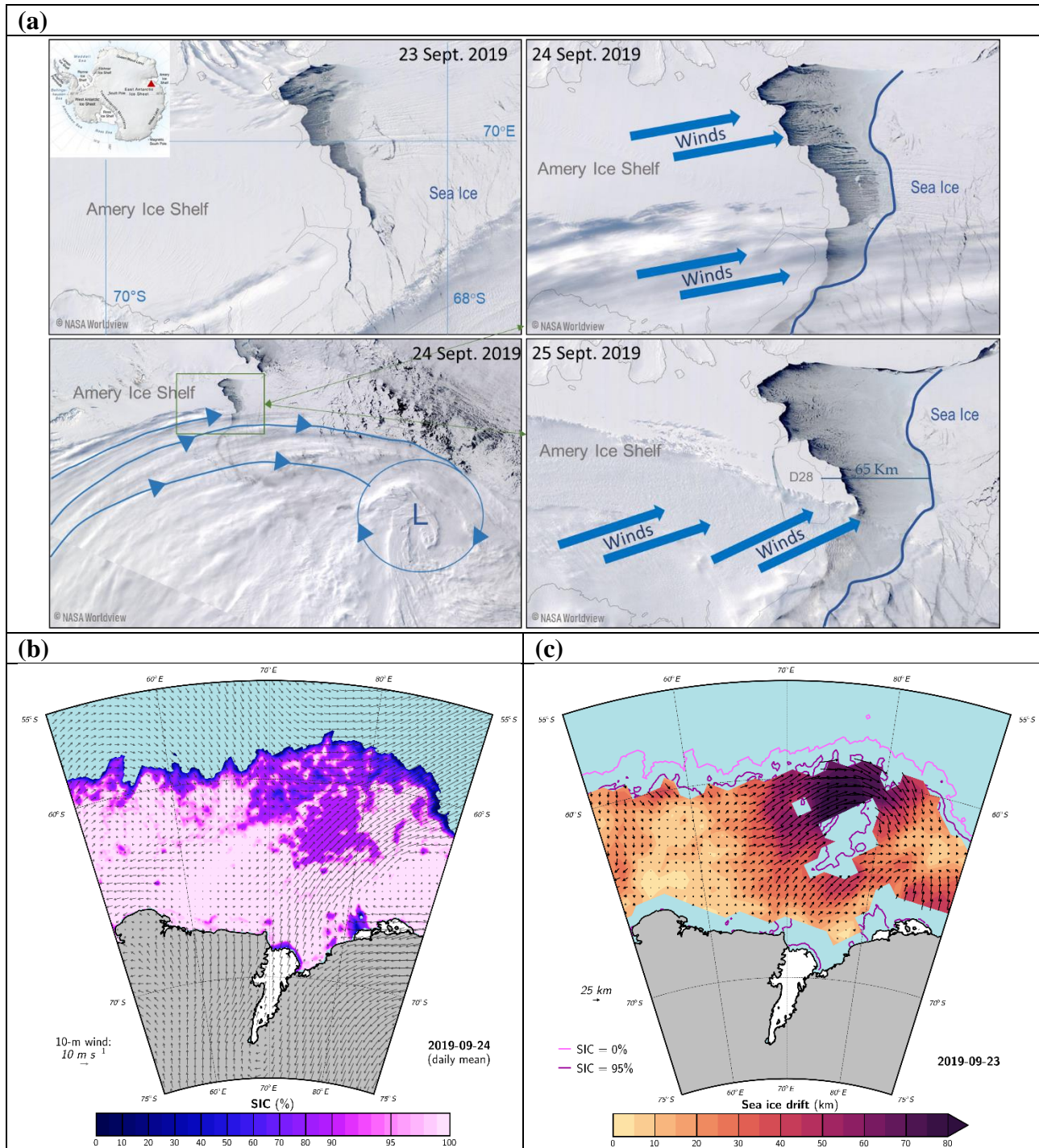394 and ultimately triggered the calving on 25 September 2019.

Figure 8: (a) MODIS satellite visible imagery of the Amery Ice Shelf showing the ice shelf before the calving on 23 September 2019, during the calving on 24-25 September 2019. Image credit:

NASA Worldview. (b) Satellite-derived sea ice concentrations and ERA5-derived daily mean 10-m winds in vectors over 55-75S and 50-90E on 24 September 2019 at 0000 UTC. (c) Satellite-derived daily sea-ice drift velocity in colors and direction in vectors on 23 September 2019. The solid pink contour is the 0% sea ice concentration contour and the solid purple contour is the 95% sea ice concentration contour.

395

3. Discussion and conclusions

397   In this study, the role of atmospheric extremes in the recent calving of the Amery Ice Shelf in
398 September 2019 is addressed by investigating the atmospheric conditions in combination with the
399 ice and ocean state. During the month of September 2019, the circulation around Antarctica was
400 characterized by anomalously-pronounced 3 ridges and 3 troughs with the Indian sector of the
401 Southern Ocean being under the influence of troughing and surrounded by two blocking ridges;
402 one over the southern Atlantic to the west and one over Davis Sea and southern Australia to the
403 east.

404   During the second half of September 2019, a series of explosive polar cyclones, evolving into
405 stationary twin polar cyclones, impacted the region of the Amery Ice Shelf. The first explosive
406 cyclone occurred on 18 September 2019 and evolved into two stationary twin polar cyclones on
407 19-22 September 2019 sitting to the west of the ice shelf. The second explosive cyclone formed
408 on 23 September 2019 and evolved into two stationary twin polar cyclones on 24-25 September
409 2019, sitting, this time, to the east of the Amery Ice Shelf. Both explosive-cyclone episodes were
410 accompanied by intense atmospheric rivers bringing anomalous warm and moist air masses
411 poleward. The stationary aspect of the deep cyclones had a large impact on the ice conditions as it
412 subjected the ice to sustained stress and strain. The main difference between the two episodes is
413 the location at which the twin cyclones were stationary, relative to the Amery Ice Shelf, which
414 determined the characteristics of the air masses and the wind direction that affected the ice shelf.
415 This position of the cyclones relative to the Amery Ice Shelf was, in turn, determined in each
416 episode, by the location of the blocking ridges in the general circulation.

417   During the first episode, anomalous warm, moist and easterly winds impacted the ice shelf and
418 surrounding sea ice, whereas during the second episode, the ice shelf and surrounding sea ice were
419 under the influence of anomalous westerlies. The first episode resulted in a shoreward storm surge
420 at the front of the ice shelf. During the second episode, anomalously strong offshore winds resulted
421 in an ocean ward slope and an ice-free area in front of the western side of the ice shelf. The
422 sustained strong winds and associated sea surface slope toward the open ocean maintained a strain
423 on the shelf-front and amplified the fracture along the pre-existing rift leading to the calving.

424   The detached iceberg after calving followed a northeasterly motion being dragged by the
425 prevailing winds and associated ocean currents. This drifting direction was similar to the one
426 followed by the sea ice one day before and gave an indication of the impact of the wind direction
427 on this process. Given the east-exposed orientation of the crack at the ice shelf-front, the direction
428 of the sustained strong westerly winds was deterministic for the calving.

In summary, atmospheric forcings by the explosive twin polar cyclones induced a gravitationally-driven calving at the Amery Ice Shelf in September 2019 via storm tide and subsequent ocean ward sea-surface slope.

The analysis of this unique event could help better understand the underlying factors triggering the calving of ice shelves and hence improve the modelling capabilities of ice shelf future evolution their possible contribution to sea level rise. Our analysis highlights the need for ice sheet models, used to project sea level rise, to account for atmospheric forcing at high resolution, in addition to sea ice and ocean waves, if they were to simulate accurately the changes occurring in the ice sheet and glaciers and their contribution to sea level rise.

In fact, important changes in the atmospheric circulation are being observed in the Southern Hemisphere. For instance, between 1979 and 2010 the subtropical jet streams moved poleward by 6.5 ± 0.2 degrees in the Southern Hemisphere (Hudson, 2012) and the westerlies strengthened and shifted poleward (Fogt and Marshal, 2020). The observed poleward movement over the past few decades represents a significant change in the position of the sub-tropical jet stream, which should lead to significant latitudinal shifts in the global weather patterns, the hydrological cycle and their impact on Antarctic ice shelves.

The variability of the polar jet front in the Southern Hemisphere and whether similar behavior as the polar jet in the Northern Hemisphere is underway around Antarctica needs to be investigated in future work. Several studies have shown evidence for a wavier jet stream in response to rapid Arctic warming and reported a weakening of the polar jet as a result of a reduced temperature gradient between high and mid-latitudes due to the increased temperatures in the Arctic (e.g., Francis and Vavrus, 2015; Coumou et al., 2015; Mann et al., 2017). Such change in the polar jet, which acts as an isolation boundary between high and mid latitudes, would lead to more interactions, and spark feedback mechanisms between the Antarctic system and mid-latitudes as it happened to be the case in the Arctic (Francis et al., 2018; 2019b).

The poleward shift of the cyclones together with the decrease in sea ice extent in recent years makes it more urgent to assess the impact of cyclones on Antarctic-wide maritime-terminating ice shelves as higher numbers of large cyclones could be expected to reach further south and therefore affects ice shelves dynamics. If extreme polar cyclones are to form or reach more frequently ice shelves due to climate change, their destructive effect may have important consequences and needs to be accounted for in models used for sea level and Antarctic Ice Sheet mass balance projections.

4. Data and methods

The atmospheric analysis is based on data from the ERA5 reanalysis (Hersbach et al., 2020). During the period 16-25 September 2019, hourly maps of mean sea level pressure (MSLP), winds, 2m temperature and total column water vapor (TCWV) are analyzed. Furthermore, in order to investigate the anomalous character of the atmospheric conditions, we calculated, for the same period and quantities listed above, hourly standardized anomalies and percentile ranks relative to all hourly ERA5 September values during the full record (1979-2019) over the area 45-95°E, 50-75°S. In addition, a histogram analysis has been performed over a smaller domain limited to the ice-shelf front area and adjacent mouth of Prydz Bay (i.e., 70-65°S and 70-75°E). The histograms

469 represent the distribution of hourly values spatially averaged over this domain, for all months
470 during 1979-2019.

471 Daily sea ice extent and concentration data are derived from the AMSR-E / AMSR2 unified record
472 (Meier et al., 2018) at 12.5 km spatial resolution (https://nsidc.org/data/AU_SI12/versions/1). To
473 check the motion in the sea ice field in the Amery Basin, we used the low-resolution sea ice drift
474 product of the EUMETSAT Ocean and Sea Ice Satellite Application Facility (OSI SAF, www.osi-
475 saf.org). This is a 48-hour average gridded ice drift dataset processed on a daily basis and made
476 available on a 62.5 km Polar Stereographic Grid (e.g., Kwok et al. 2017). Ice motion vectors are
477 estimated by an advanced cross-correlation method on pairs of satellite images (Lavergne et al.,
478 2010). It uses the multi-sensor spatial covering product that combines SSMIS (91 GHz H and V
479 polarization) on board DMSP platform F17, ASCAT (C-band backscatter) on board EUMETSAT
480 platform Metop-A, and AMSR-2 on board JAXA platform GCOM-W. Due to atmospheric noise
481 and surface melting these data are only available for the Southern Hemisphere winter (1st April to
482 31st October).

483 Visible imagery of the Amery Ice Shelf and surrounding area are taken from MODIS/VIIRS land
484 products (ORNL DAAC, 2018) using the NASA Worldview application
485 (https://worldview.earthdata.nasa.gov).

486 Sentinel-1 data has been used to determine potential surface melt (e.g., Datta et. al, 2019) and to
487 track ice velocity over the Amery ice shelf prior to the D28 iceberg calving by using feature
488 tracking in ESA's SNAP Sentinel-1 toolbox. Sentinel-3A and 3B data were used via the ESA
489 Ocean Virtual Laboratory application to determine the wave height at the front of the Amery Ice
490 Shelf.

491 The ocean slope and elevation are taken from the Hybrid Coordinate Ocean Model (HYCOM,
492 https://www.hycom.org/). HYCOM (Cummings and Smedstad, 2013) is a data-assimilative hybrid
493 isopycnal-sigma-pressure (generalized) coordinate ocean model of which we downloaded
494 elevation from the Google Earth Engine at 0.08-degree latitude/longitude grid. Based on this
495 elevation dataset, the surface slope was derived as the local gradient using the 4-connected
496 neighbors of each pixel.

Acknowledgments

504 **Code and Data availability:** All data needed to evaluate the conclusions in the paper are present
505 in the paper. Correspondence and requests for materials should be addressed to DF.

Author contributions D.F. conceived the study and wrote the initial manuscript. K.M. analyzed the satellite and reanalysis data. S.L analyzed satellite data. M.T. and P.H. provided input on result analysis. All authors interpreted results and provided input to the final manuscript.

Competing Interests The authors declare that they have no competing interests.

References

1. Allen, J.T., Pezza, A. B., and Black, M. T. (2010) Explosive cyclogenesis: a global climatology comparing multiple reanalyses. Journal of Climate, v.23, 6468–6484.
2. Aitken, A., Roberts, J., Ommen, T. et al. Repeated large-scale retreat and advance of Totten Glacier indicated by inland bed erosion. Nature 533, 385–389 (2016). https://doi.org/10.1038/nature17447.
3. Barnes, E. A., and L. Polvani (2013), Response of the midlatitude jets, and of their variability, to increased greenhouse gases in the CMIP5 Models, J. Clim., 26, 7117– 7135.
4. Bassis, J., Fricker, H., Coleman, R., & Minster, J. (2008). An investigation into the forces that drive ice-shelf rift propagation on the Amery Ice Shelf, East Antarctica. Journal of Glaciology, 54(184), 17-27. doi:10.3189/002214308784409116.
5. Bassis, J. N. and Ma, Y.: Evolution of basal crevasses links ice shelf stability to ocean forcing, Earth Planet. Sci. Lett., 409, 203–211, https://doi.org/10.1016/j.epsl.2014.11.003, 2015.
6. Bengtsson, L., K. I. Hodges, and N. Keenlyside (2009), Will extratropical storms intensify in a warmer climate? J. Clim., 22(9), 2276– 2301.
7. Benn D. I. and J. A. Åström (2018) Calving glaciers and ice shelves, Advances in Physics: X, 3:1, DOI: 10.1080/23746149.2018.1513819.
8. Bromirski, P. D., Sergienko, O. V. & MacAyeal, D. R. Transoceanic infragravity waves impacting Antarctic ice shelves. Geophys. Res. Lett. 37, L02502 (2010).
9. Brunt, K., Okal, E., & MacAyeal, D. (2011). Antarctic ice-shelf calving triggered by the Honshu (Japan) earthquake and tsunami, March 2011. Journal of Glaciology, 57(205), 785-788. doi:10.3189/002214311798043681.
10. Chang, E. K. M., Y. Guo, and X. Xia (2012), CMIP5 multimodel ensemble projection of storm track change under global warming, J. Geophys. Res., 117, D23118, doi:10.1029/2012JD018578.
11. Chang, E. K. M., 2017: Projected Significant Increase in the Number of Extreme Extratropical Cyclones in the Southern Hemisphere. J. Climate, 30, 4915–4935, https://doi.org/10.1175/JCLI-D-16-0553.1.
12. Cook, A. J. and Vaughan, D. G.: Overview of areal changes of the ice shelves on the Antarctic Peninsula over the past 50 years, The Cryosphere, 4, 77–98, https://doi.org/10.5194/tc-4-77-2010, 2010.
13. Coumou D., J. Lehmann, J. Beckmann, (2015), The weakening summer circulation in the Northern Hemisphere mid-latitudes, Science, Vol. 348, Issue 6232, pp. 324-327. DOI: 10.1126/science.1261768.
14. Cummings, J.A. and O.M. Smedstad, 2013: Variational data analysis for the global ocean. In: S.K. Park and L. Xu (Eds.), Data Assimilation for Atmospheric, Oceanic and Hydrologic

Applications Vol. II., DOI 10.1007/978-3-642-35088-7_13, Springer-Verlag Berlin Heidelberg.

15. Datta, R. T. Tedesco, M., Fettweis, X., Agosta, C., Lhermitte, S., Lenaerts, J.T.M., Wever, N. (2019) The Effect of Foehn-Induced Surface Melt on Firn Evolution Over the Northeast Antarctic Peninsula. Geophys. Res. Lett. 46, 3822–383, doi: 10.1029/2018GL080845.

16. Davies, H. C., 1997: Emergence of the mainstream cyclogenesis theories. Meteor. Z.,6, 261–274.

17. DeConto, R., Pollard, D. Contribution of Antarctica to past and future sea-level rise. Nature 531, 591–597 (2016), https://doi.org/10.1038/nature17145.

18. Dolatshah, A., Nelli, F., Alberello, A., Bruneau, L., Bennetts, L. G., Meylan, M. H., Monty, J. P., and Toffoli, A. "Wave Attenuation due to Ice Cover: An Experimental Model in a Wave-Ice Flume." Proceedings of the ASME 2017 36th International Conference on Ocean, Offshore and Arctic Engineering. Volume 8: Polar and Arctic Sciences and Technology; Petroleum Technology. Trondheim, Norway. June 25–30, 2017. V008T07A016. ASME. https://doi.org/10.1115/OMAE2017-61548.

19. Darji S., S.R. Oza, R. D. Shah, B. P. Rathore and I. M. Bahuguna, 2018: Rift assessment and potential calving zone of Amery Ice Shelf, East Antarctica. Current Science, 115, 1799-1804, doi: 10.18520/cs/v115/i9/1799-1804.

20. Eayrs, C., Holland, D. M., Francis, D., Wagner, T. J. W., Kumar, R., & Li, X. (2019). Understanding the seasonal cycle of Antarctic sea ice extent in the context of longer-term variability. Reviews of Geophysics. 57, 1037– 1064, https://doi.org/10.1029/2018RG000631.

21. Ferreira, R. N., W. N.Schubert, and J. J.Hack, 1996: Dynamical aspects of twin tropical cyclones associated with the Madden–Julian oscillation.J. Atmos. Sci., 53, 929–945.

22. Francis J. A. and S. J. Vavrus, 2015, Evidence for a wavier jet stream in response to rapid Arctic warming, Environ. Res. Lett. 10 014005.

23. Francis D., C. Eayrs, J-P. Chaboureau, T. Mote, D. Holland (2018), "Polar jet associated circulation triggered a Saharan cyclone and derived the poleward transport of the African dust generated by the cyclone" Journal of Geophysical Research: Atmospheres. DOI:10.1029/2018JD029095.

24. Francis D., C. Eayrs, J. Cuesta, D. Holland (2019a), Polar cyclones at the origin of the reoccurrence of the Maud Rise Polynya in austral winter 2017, Journal of Geophysical Research: Atmospheres,124. https://doi.org/10.1029/2019JD030618, 2019.

25. Francis D., C. Eayrs, J-P. Chaboureau, T. Mote, D. Holland (2019b), A meandering polar jet caused the development of a Saharan cyclone and the transport of dust toward Greenland, Adv. Sci. Res., 1, 1–8, https://doi.org/10.5194/asr-16-49-2019, 2019.

26. Francis D., K.S. Mattingly, N. Alshamsi, M. Temimi, R. Massom, P. Heil, 2020, On the crucial role of atmospheric rivers in the two major Weddell Polynya events in 1973 and 2017 in Antarctica. Sci. Adv. 6, eabc2695 (2020). https://advances.sciencemag.org/content/6/46/eabc2695.

27. Fricker, H., Young, N., Allison, I., & Coleman, R. (2002). Iceberg calving from the Amery Ice Shelf, East Antarctica. Annals of Glaciology, 34, 241-246. doi:10.3189/172756402781817581

588   28. Fricker, H. A., N. W. Young, R. Coleman, J. N. Bassis, and J.-B. Minster (2005), Multi-year
589   monitoring of rift propagation on the Amery Ice Shelf, East Antarctica, Geophys. Res. Lett.,
590   32, L02502, doi:10.1029/2004GL021036.
591   29. Fogt, RL, Marshall, GJ. The Southern Annular Mode: Variability, trends, and climate impacts
592   across the Southern Hemisphere. WIREs Clim Change. 2020; 11:e652.
593   https://doi.org/10.1002/wcc.652
594   30. Fyfe, J. C. (2003), Extratropical Southern Hemisphere cyclones: Harbingers of climate
595   change?, J. Clim., 16, 2802– 2805.
596   31. Galton-Fenzi, B. K., J. R. Hunter, R. Coleman, S. J. Marsland, and R. C. Warner (2012),
597   Modeling the basal meltingand marine ice accretion of the Amery Ice Shelf, J. Geophys. Res.,
598   117, C09031, doi:10.1029/2012JC008214.
599   32. Greenbaum, J., Blankenship, D., Young, D. et al. Ocean access to a cavity beneath Totten
600   Glacier in East Antarctica. Nature Geosci 8, 294–298 (2015).
601   https://doi.org/10.1038/ngeo2388.
602   33. Grieger J., G. C. Leckebusch, C. C. Raible, I. Rudeva & I. Simmonds (2018) Subantarctic
603   cyclones identified by 14 tracking methods, and their role for moisture transports into the
604   continent, Tellus A: Dynamic Meteorology and Oceanography, 70:1, 1-18, DOI:
605   10.1080/16000870.2018.1454808.
606   34. Hersbach, H., B. Bell, P. Berrisford, et al., 2020: The ERA5 global reanalysis. Quarterly
607   Journal of the Royal Meteorological Society, 146, 1999–2049, doi: 10.1002/qj.3803.Hogg, A.,
608   Gudmundsson, G. Impacts of the Larsen-C Ice Shelf calving event. Nature Clim Change 7,
609   540–542 (2017). https://doi.org/10.1038/nclimate3359.
610   35. Holdsworth, G. & Glynn, J. Iceberg calving from floating glaciers by a vibration mechanism.
611   Nature 274, 464–466 (1978).
612   36. Hudson, R. D.: Measurements of the movement of the jet streams at mid-latitudes, in the
613   Northern and Southern Hemispheres, 1979 to 2010, Atmos. Chem. Phys., 12, 7797–7808,
614   https://doi.org/10.5194/acp-12-7797-2012, 2012.
615   37. Irving, D., & Simmonds, I. (2015). A Novel Approach to Diagnosing Southern Hemisphere
616   Planetary Wave Activity and Its Influence on Regional Climate Variability, Journal of Climate,
617   28(23), 9041-9057. Retrieved Jan 28, 2021, from
618   https://journals.ametsoc.org/view/journals/clim/28/23/jcli-d-15-0287.1.xml.
619   38. Jeong, S., I. M. Howat, and J. N. Bassis (2016), Accelerated ice shelf rifting and retreat at Pine
620   Island Glacier, WestAntarctica, Geophys. Res. Lett., 43,11,720–11,725,
621   doi:10.1002/2016GL071360.
622   39. King, M. A., R. Coleman, A.-J. Freemantle, H. A. Fricker, R. S. Hurd, B. Legrésy, L. Padman,
623   and R. Warner (2009), A 4-decade record of elevation change of the Amery Ice Shelf, East
624   Antarctica, J. Geophys. Res., 114, F01010, doi:10.1029/2008JF001094.
625   40. Kohout, A., Williams, M., Dean, S. et al. Storm-induced sea-ice breakup and the implications
626   for ice extent. Nature 509, 604–607 (2014). https://doi.org/10.1038/nature13262
627   41.
628   42. Kwok, R., Pang, S. S., and Kacimi, S.: Sea ice drift in the Southern Ocean: Regional patterns,
629   variability and trends, Elem. Sci. Anth., 5, 1–16, https://doi.org/10.1525/elementa.226, 2017.

630   43. Lambert, S. J., and J. C. Fyfe (2006), Changes in winter cyclone frequencies and strengths
631   simulated in enhanced greenhouse warming experiments: Results from the models
632   participating in the IPCC diagnostic exercise, Clim. Dyn., 26, 713– 728.
633   44. Lavergne, T., Eastwood, S., Teffah, Z., Schyberg, H., and Breivik, L.-A. (2010), Sea ice
634   motion from low-resolution satellite sensors: An alternative method and its validation in the
635   Arctic, J. Geophys. Res., 115, C10032, doi:10.1029/2009JC005958.
636   45. Lee, S., Gong, T., Feldstein, S. B., Screen, J. A., & Simmonds, I. (2017). Revisiting the cause
637   of the 1989–2009 Arctic surface warming using the surface energy budget: Downward infrared
638   radiation dominates the surface fluxes. Geophysical Research Letters, 44, 10,654– 10,661.
639   https://doi.org/10.1002/2017GL075375.
640   46. Lim, Eun-Pa; Simmonds, Ian (2002). Explosive Cyclone Development in the Southern
641   Hemisphere and a Comparison with Northern Hemisphere Events. Monthly Weather Review.
642   130 (9): 2188–2209. Bibcode:2002 MWRv. .130.2188L. doi:10.1175/1520-
643   0493(2002)130<2188:ECDITS>2.0.CO;2.
644   47. Liu Y., J. C. Moore, X. Cheng, R. M. Gladstone, J. N. Bassis, H. Liu, J. Wen, F. Hui, 2015,
645   Iceberg calving of Antarctic ice shelves, Proceedings of the National Academy of Sciences,
646   March 2015, 112 (11) 3263-3268; DOI: 10.1073/pnas.1415137112.
647   48. Mann, M., Rahmstorf, S., Kornhuber, K. et al. Influence of Anthropogenic Climate Change on
648   Planetary Wave Resonance and Extreme Weather Events. Sci Rep 7, 45242 (2017).
649   https://doi.org/10.1038/srep45242
650   49. Massom, R.A., Scambos, T.A., Bennetts, L.G. et al. Antarctic ice shelf disintegration triggered
651   by sea ice loss and ocean swell. Nature 558, 383–389 (2018). https://doi.org/10.1038/s41586-
652   018-0212-1.
653   50. Matear, R., O'Kane, T., Risbey, J. et al. Sources of heterogeneous variability and trends in
654   Antarctic sea-ice. Nat Commun 6, 8656 (2015). https://doi.org/10.1038/ncomms9656.
655   51. Meier, W. N., T. Markus, and J. C. Comiso. 2018. AMSR-E/AMSR2 Unified L3 Daily 12.5
656   km Brightness Temperatures, Sea Ice Concentration, Motion & Snow Depth Polar Grids,
657   Version 1. [Antarctica]. Boulder, Colorado USA. NASA National Snow and Ice Data Center
658   Distributed Active Archive Center. doi: https://doi.org/10.5067/RA1MIJOYPK3P [10 April
659   2020].
660   52. Morrison K.A., A. M. Hogg, M.H. England and P. Spence Warm Circumpolar Deep Water
661   transport toward Antarctica driven by local dense water export in canyons, Science Advances,
662   2020: Vol. 6, no. 18, eaav2516, DOI: 10.1126/sciadv.aav2516.
663   53. Moustaoui, M., H. Teitelbaum, C. Basdevant, and Y. Boughaleb, Linked behavior of twin
664   tropical cyclones, J. Geophys. Res., 107(D19), 4378, doi:10.1029/2000JD000066, 2002.
665   54. Neu, U., Akperov, M. G., Bellenbaum, N., Benestad, R., Blender, R., Caballero, R., Cocozza,
666   A., Dacre, H. F., Feng, Y., Fraedrich, K., Grieger, J., Gulev, S., Hanley, J., Hewson, T., Inatsu,
667   M., Keay, K., Kew, S. F., Kindem, I., Leckebusch, G. C., Liberato, M. L. R., Lionello, P.,
668   Mokhov, I. I., Pinto, J. G., Raible, C. C., Reale, M., Rudeva, I., Schuster, M., Simmonds, I.,
669   Sinclair, M., Sprenger, M., Tilinina, N. D., Trigo, I. F., Ulbrich, S., Ulbrich, U., Wang, X. L.,
670   & Wernli, H. (2013). IMILAST: A Community Effort to Intercompare Extratropical Cyclone
671   Detection and Tracking Algorithms, Bulletin of the American Meteorological Society, 94(4),

529-547. Retrieved Jan 28, 2021, from https://journals.ametsoc.org/view/journals/bams/94/4/bams-d-11-00154.1.xml.

55. ORNL DAAC. 2018. MODIS and VIIRS Land Products Global Subsetting and Visualization Tool. ORNL DAAC, Oak Ridge, Tennessee, USA. Accessed May 20, 2020. Subset obtained for MOD13Q1 product over the Amery Ice Shelf – Antarctica, time period: 2019-09-01 to 2019-09-30. https://doi.org/10.3334/ORNLDAAC/1379.

56. Pezza, A.B., Simmonds, I. and Renwick, J.A. (2007), Southern hemisphere cyclones and anticyclones: recent trends and links with decadal variability in the Pacific Ocean. Int. J. Climatol., 27: 1403-1419. https://doi.org/10.1002/joc.1477.

57. Pope, J. O., Holland, P. R., Orr, A., Marshall, G. J., and Phillips, T. (2017), The impacts of El Niño on the observed sea ice budget of West Antarctica, Geophys. Res. Lett., 44, 6200– 6208, doi:10.1002/2017GL073414.

58. Pritchard, H. D., Ligtenberg S.R., Fricker H.A., Vaughan D.G., van den Broeke MR, Padman L., Antarctic ice-sheet loss driven by basal melting of ice shelves. Nature 484, 502–505 (2012).

59. Reale M., M. L.R. Liberato, P. Lionello, J. G. Pinto, S. Salon & S. Ulbrich (2019) A Global Climatology of Explosive Cyclones using a Multi-Tracking Approach, Tellus A: Dynamic Meteorology and Oceanography, 71:1, DOI: 10.1080/16000870.2019.1611340.

60. Raphael, M. N., 2007, The influence of atmospheric zonal wave three on Antarctic sea ice variability, J. Geophys. Res., 112, D12112, https://doi.org/10.1029/2006JD007852, 2007.

61. Renfrew A.I., G.W.K. Moore and A.A. Clerk (1997) Binary interactions between polar lows, Tellus A: Dynamic Meteorology and Oceanography, 49:5, 577-594, DOI: 10.3402/tellusa.v49i5.14823.

62. Rignot, E. et al. Accelerated ice discharge from the Antarctic Peninsula following the collapse of Larsen B ice shelf. Geophys. Res. Lett. 31, https://doi. org/10.1029/2004gl020697 (2004).

63. Rignot E., J. Mouginot, B. Scheuchl, M. van den Broeke, M. J. van Wessem, M. Morlighem, 2019, Four decades of Antarctic Ice Sheet mass balance from 1979–2017, Proceedings of the National Academy of Sciences Jan 2019, 116 (4) 1095-1103; DOI: 10.1073/pnas.1812883116.

64. Robinson, W. & Haskell, T. G. Calving of Erebus Glacier tongue. Nature 346, 615–616 (1990).

65. Robinson, W. & Haskell, T. G. Travelling flexural waves in the Erebus Glacier Tongue, McMurdo Sound, Antarctica. Cold Reg. Sci. Technol. 20, 289–293 (1992).

66. Rudeva I., I. Simmonds, Variability and trends of global atmospheric frontal activity and links with large-scale modes of variability. J. Climate 28, 3311–3330 (2015).

67. Sanders, Frederick; Gyakum, John R (1980). "Synoptic-Dynamic Climatology of the 'Bomb'". Monthly Weather Review. 108 (10): 1589–606. Bibcode:1980 MWRv.108.1589S. doi:10.1175/1520-0493(1980)108<1589:SDCOT>2.0.CO;2.

68. Scambos, T. A., Bohlander, J. A., Shuman, C. A. & Skvarca, P. Glacier acceleration and thinning after ice shelf collapse in the Larsen B embayment, Antarctica. Geophys. Res. Lett. 31,1 –4 (2004).

69. Scambos, T., Ross, R., Bauer, R., Yermolin, Y., Skvarca, P., Long, D., Bohlander, J. and Haran, T., 2008. Calving and ice-shelf break-up processes investigated by proxy: Antarctic tabular iceberg evolution during northward drift. Journal of Glaciology, 54(187), pp.579-591.

70. Scambos, T. A., Berthier, E., Haran, T., Shuman, C. A., Cook, A. J., Ligtenberg, S. R. M., and Bohlander, J.: Detailed ice loss pattern in the northern Antarctic Peninsula: widespread decline

715   driven by ice front retreats, The Cryosphere, 8, 2135–2145, https://doi.org/10.5194/tc-8-2135-
716   2014, 2014.

717 71. Schemm, S. (2018), Regional trends in weather systems help explain Antarctic sea ice trends.
718   Geophysical Research Letters, 45, 7165–7175.https://doi.org/10.1029/2018GL079109.

719 72. Schlosser E., J.G. Powers, M.G. Duda, K.W. Manning (2011) Interaction between Antarctic
720   sea ice and synoptic activity in the circumpolar trough: implications for ice-core interpretation,
721   Annals of Glaciology 52(57) 2011.

722 73. Schlosser E., F. A. Haumann, M. N. Raphael Atmospheric influences on the anomalous 2016
723   Antarctic sea ice decay (2018), The Cryosphere, 12, 1103–1119, 2018,
724   https://doi.org/10.5194/tc-12-1103-2018.

725 74. Schossler, V., Aquino, F.E., Reis, P.A. et al. Antarctic atmospheric circulation anomalies and
726   explosive cyclogenesis in the spring of 2016. Theor Appl Climatol (2020).
727   https://doi.org/10.1007/s00704-020-03200-9.

728 75. Shepherd, A., Fricker, H. A. & Farrell, S. L. Trends and connections across the Antarctic
729   cryosphere. Nature 558, 223–232 (2018).

730 76. Shimada, U., A. Wada, K. Yamazaki, N. Kitabatake (2014) Roles of an upper-level cold vortex
731   and low-level baroclinicity in the development of polar lows over the Sea of Japan, Tellus A:
732   Dynamic Meteorology and Oceanography, 66:1, DOI: 10.3402/tellusa.v66.24694.

733 77. Smith, J.A., Graham, A.G.C., Post, A.L. et al. The marine geological imprint of Antarctic ice
734   shelves. Nat Commun 10, 5635 (2019). https://doi.org/10.1038/s41467-019-13496-5.

735 78. Son, S.-W., L. M. Polvani, D. W. Waugh, H. Akiyoshi, R. Garcia, D. Kinnison, S. Pawson, E.
736   Rozanov, T. G. Shepherd, and K. Shibata (2008), The impact of stratospheric ozone recovery
737   on the Southern Hemisphere westerly jet, Science, 320, 1486– 1489.

738 79. Squire, V. A., Robinson, W. H., Meylan, M. H. & Haskell, T. G. Observations of flexural
739   waves in the Erebus Glacier Tongue, McMurdo Sound, Antarctica, and nearby sea ice. J.
740   Glaciol. 40, 377–385 (1994).

741 80. Stoll P.J., Graversen RG., Noer G, Hodges K. An objective global climatology of polar lows
742   based on reanalysis data. QJRMeteorol.Soc.2018;144:2099–2117.
743   https://doi.org/10.1002/qj.3309

744 81. Swart S., E. C. Cambell, C. H. Heuze, K. Johnson, J. L. Lieser, R. Masson, M. Mazloff, M.
745   Meredith, P. Reid, J.-B. Sallee, S. Stammerjohn (2018) Litmus or sea ice anomaly? Sidebar,
746   State of the Climate, BAMS, August 2018, DOI:10.1175/BAMS-D-18-0173.1.

747 82. Tamarin, T., and Y. Kaspi (2017), The poleward shift of storm tracks under global warming:
748   A Lagrangian perspective, Geophys. Res. Lett., 44, 10,666–10,674,
749   doi:10.1002/2017GL073633.

750 83. Li T., Y. Liu and X. Cheng, 2020: Recent and imminent calving events do little to impair
751   Amery ice shelf's stability. Acta Oceanologica Sinica, 39, 168-170, doi: 10.1007/s13131-020-
752   1600-6.

753 84. Turner J., S.A. Harangozo, G.J. Marshall, J.C. King, S.R. Colwell (2002) Anomalous
754   atmospheric circulation over the Weddell Sea, Antarctica during the Austral summer of
755   2001/02 resulting in extreme sea ice conditions, Geophys.Res. Lett.,, Vol. 29, N0. 24, 2160,
756   doi:10.1029/2002GL015565, 2002.

85. Uccellini L.W. (1990) Processes Contributing to the Rapid Development of Extratropical Cyclones. In: Newton C.W., Holopainen E.O. (eds) Extratropical Cyclones. American Meteorological Society, Boston, MA.

86. Ulbrich, U., Leckebusch, G. C., Grieger, J., Schuster, M.,Akperov, M., Bardin, M. Y., Feng, Y., Gulev, S., Inatsu, M., Keay, K., Kew, S. F., Liberato, M. L. R., Lionello, P., Mokhov, I. I., Neu, U., Pinto, J. G., Raible, C. C., Reale, M., Rudeva, I., Simmonds, I., Tilinina, N. D., Trigo, I. F., Ulbrich, S., Wang, X. L. and Wernli, H. (2013) Are greenhouse gas signals of Northern Hemisphere winter extra-tropical cyclone activity dependent on the identification and tracking algorithm? Meteorologische Zeitschrift, 22 (1). pp. 61-68. ISSN 0941-2948. doi: https://doi.org/10.1127/0941-2948/2013/0420.

87. Uotila, P., T. Vihma, A. B. Pezza, I. Simmonds, K. Keay, and A. H. Lynch (2011), Relationships between Antarctic cyclones and surface conditions as derived from high-resolution numerical weather prediction data, J. Geophys. Res., 116, D07109, doi:10.1029/2010JD015358.

88. Vaughan, D. G., H. F. J. Corr, R. A. Bindschadler, P. Dutrieux, G. H. Gudmundsson, A. Jenkins, T. Newman, P. Vornberger, and D. J. Wingham (2012), Subglacial melt channels and fracture in the floating part of Pine Island Glacier, Antarctica, J. Geophys. Res., 117, F03012, doi:10.1029/2012JF002360.

89. Vernon A. Squire, 2020: Ocean wave interactions with sea ice: A reappraisal. Annual Review of Fluid Mechanics, 52, 37-60, doi: 10.1146/annurev-fluid-010719-060301.

90. Vichi, M., Eayrs, C., Alberello, A., Bekker, A., Bennetts, L., Holland, D., et al. (2019). Effects of an explosive polar cyclone crossing the Antarctic marginal ice zone. Geophysical Research Letters, 46, 5948–5958. https://doi.org/ 10.1029/2019GL082457.

91. Wagner J.S., A. Gohm, A. Dörnbrack, A. Schäfler (2011), The mesoscale structure of a polar low: airborne lidar measurements and simulations. Q. J. R. Meteorol. Soc. DOI: 10.1002/qj.857.

92. Watanabe, S. I., and H. Niino, 2014: Genesis and Development Mechanisms of a Polar Mesocyclone over the Japan Sea. Mon. Wea. Rev., 142, 2248–2270, https://doi.org/10.1175/MWR-D-13-00226.1.

93. Wei, L., Qin, T. Characteristics of cyclone climatology and variability in the Southern Ocean. Acta Oceanol. Sin. 35, 59–67 (2016). https://doi.org/10.1007/s13131-016-0913-y.

94. Wille, J. D., V. Favier, A. Dufour, I. V. Gorodetskaya, J. Turner, C. Agosta and F. Codron, 2019: West Antarctic surface melt triggered by atmospheric rivers. Nature Geoscience, 12, 911-916, doi: 10.1038/s41561-019-0460-1.

95. Woods, C., and R. Caballero, 2016: The Role of Moist Intrusions in Winter Arctic Warming and Sea Ice Decline. J. Climate, 29, 4473–4485, https://doi.org/10.1175/JCLI-D-15-0773.1.

96. Yokoyama, Y.; Yamamoto, M., 2019, Influences of surface heat flux on twin cyclone structure during their explosive development over the East Asian marginal seas on 23 January 2008. Weather Clim. Extrem. 2019, 23, 100198. https://doi.org/10.1016/j.wace.2019.100198.

97. Zhao, C., Cheng, X., Liu, Y., Hui, F., Kang, J., Wang, X., Cheng, C. (2013). The slow-growing tooth of the Amery Ice Shelf from 2004 to 2012. Journal of Glaciology, 59(215), 592-596. doi:10.3189/2013JoG12J225.